EUROPEAN ORGANISATION FOR NUCLEAR RESEARCH (CERN)

Submitted to: JHEP

CERN-EP-2022-249
10th January 2023

Search for leptonic charge asymmetry in $t\bar{t}W$ production in final states with three leptons at $\sqrt{s} = 13$ TeV

The ATLAS Collaboration

A search for the leptonic charge asymmetry (A_{c}^{ℓ}) of top-quark–antiquark pair production in association with a W boson ($t\bar{t}W$) is presented. The search is performed using final states with exactly three charged light leptons (electrons or muons) and is based on $\sqrt{s} = 13$ TeV proton–proton collision data collected with the ATLAS detector at the Large Hadron Collider at CERN during the years 2015–2018, corresponding to an integrated luminosity of 139 fb^{-1}. A profile-likelihood fit to the event yields in multiple regions corresponding to positive and negative differences between the pseudorapidities of the charged leptons from top-quark and top-antiquark decays is used to extract the charge asymmetry. At reconstruction level, the asymmetry is found to be -0.123 ± 0.136 (stat.) $\pm\, 0.051$ (syst.). An unfolding procedure is applied to convert the result at reconstruction level into a charge-asymmetry value in a fiducial volume at particle level with the result of -0.112 ± 0.170 (stat.) $\pm\, 0.054$ (syst.). The Standard Model expectations for these two observables are calculated using Monte Carlo simulations with next-to-leading-order plus parton shower precision in quantum chromodynamics and including next-to-leading-order electroweak corrections. They are $-0.084\,^{+0.005}_{-0.003}$ (scale) $\pm\, 0.006$ (MC stat.) and $-0.063\,^{+0.007}_{-0.004}$ (scale) $\pm\, 0.004$ (MC stat.) respectively, and in agreement with the measurements.

1 Introduction

The production of a top-quark–antiquark ($t\bar{t}$) pair in association with a W boson, commonly referred to as $t\bar{t}W$, is a rare process in the Standard Model (SM) that can be produced at the Large Hadron Collider (LHC). State-of-the-art cross-section calculations for the $t\bar{t}W$ process are especially complex, as large corrections arise from higher powers of both the strong and weak couplings [1]. Thus, measurements of the $t\bar{t}W$ process represent a sensitive test of the predictions of quantum chromodynamics (QCD) and the electroweak (EW) sector of the SM, as well as their interplay. Both the inclusive and differential cross-section measurements are very relevant, as they can provide indirect hints of new physics beyond the SM (BSM) in scenarios where at least one of the SM couplings is modified [2]. Furthermore, it can be one of the main backgrounds in searches for BSM phenomena, such as supersymmetric squark or gluino production or vector-like quarks [3, 4]. It also represents an irreducible background in many measurements of SM processes such as $t\bar{t}$ production in association with a Higgs boson ($t\bar{t}H$) or the production of four top quarks ($t\bar{t}t\bar{t}$) [5, 6]. The inclusive cross-section of $t\bar{t}W$ production has been measured by both the ATLAS and CMS collaborations at $\sqrt{s} = 13$ TeV using partial and full LHC Run 2 datasets [7, 8], respectively.

Illustrative Feynman diagrams contributing to $t\bar{t}W$ production at leading order (LO) and next-to-leading order (NLO) for both QCD and EW production are shown in Figure 1 where q' indicates a quark of different flavour from that of the other initial-state quark. At LO, only the $q\bar{q}'$ initial state is present (Figure 1 a,b). At NLO, the quark–gluon (qg) channels open up (Figure 1 c,d), whereas gluon–gluon (gg) fusion production does not contribute until next-to-next-to-leading-order (NNLO) corrections are included.

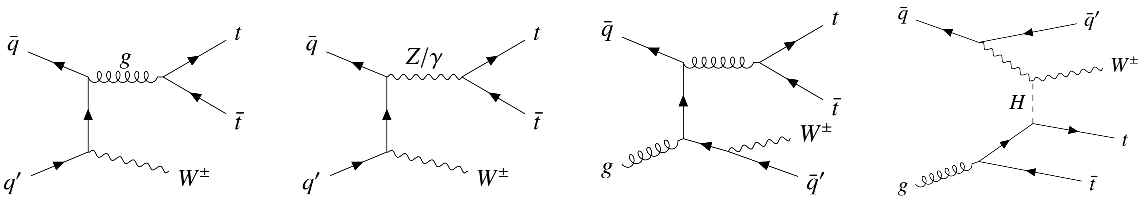

(a) (b) (c) (d)

Figure 1: Examples of Feynman diagrams of $t\bar{t}W$ production at (a,b) LO and (c,d) NLO with one extra parton. The diagrams show (a,c) QCD and (b,d) EW $t\bar{t}W$ production.

In $t\bar{t}$ production, the top quark (top antiquark) is preferentially produced in the direction of the incoming quark (antiquark). This is due to the interference effects between amplitudes in the $q\bar{q}$ initial state and results in a difference in the rapidity distribution between top quarks and top antiquarks.[1] In proton–proton (pp) collisions at the LHC, this production asymmetry results in a central–forward rapidity charge asymmetry as top quarks (antiquarks) are produced with more forward (central) rapidities. Given that $t\bar{t}$ production at the LHC is dominated by the charge-symmetric gg initial state, such asymmetry is a subtle (order of 1%) effect. At the Tevatron collider ($p\bar{p}$ collisions), the preferential direction of the incoming quark (antiquark) is very likely to coincide with that of the proton (antiproton). Thus, a forward–backward asymmetry is sizable (order of 10%).

---

[1] ATLAS uses a right-handed coordinate system with its origin at the nominal interaction point in the centre of the detector and the z-axis along the beam pipe. The x-axis points from the interaction point to the centre of the LHC ring, and the y-axis points upwards. Cylindrical coordinates (r, ϕ) are used in the transverse plane, ϕ being the azimuthal angle around the z-axis. The rapidity (y) of a particle is given by $y = 1/2\ \ln{(E + p_z)/(E - p_z)}$. The pseudorapidity ($\eta$) is defined in terms of the polar angle θ as $\eta = -\ln\tan(\theta/2)$. The angular distance is measured in units of $\Delta R \equiv \sqrt{(\Delta\eta)^2 + (\Delta\phi)^2}$.

The top-quark-based rapidity charge asymmetry ($A^t_{\mathrm{c},y}$) is defined by

$$A^t_{\mathrm{c},y} = \frac{N\,(\Delta y^t > 0) - N\,(\Delta y^t < 0)}{N\,(\Delta y^t > 0) + N\,(\Delta y^t < 0)}, \tag{1}$$

where $\Delta y^t = |y_t| - |y_{\bar{t}}|$ is the difference between the absolute rapidities of the top quark ($|y_t|$) and top antiquark ($|y_{\bar{t}}|$), respectively.

In $t\bar{t}W$ production, the relative dominance of the $q\bar{q}'$ initial state leads to a larger rapidity charge asymmetry than in $t\bar{t}$ production [9, 10]. Furthermore, the W boson present in $t\bar{t}W$ production is typically radiated from the initial $q\bar{q}'$ state and, therefore, serves as a polariser of the initial $q\bar{q}'$ state and in turn the final $t\bar{t}$ state. This polarisation further enhances the asymmetry between the decay products of the top quarks and top antiquarks. The prospects for experimental observation of these asymmetries are greatest in the case of the charged leptons originating from the top-quark (antiquark) decays. This is due to the precision with which the lepton kinematics can be reconstructed and the power with which reducible background processes can be suppressed. The leptonic charge asymmetry (A^ℓ_c), in the following just referred to as 'charge asymmetry', is defined analogously to Eq. (1), but based on the pseudorapidities of the leptons from the top-quark and top-antiquark decays:

$$A^\ell_\mathrm{c} = \frac{N\,(\Delta\eta^\ell > 0) - N\,(\Delta\eta^\ell < 0)}{N\,(\Delta\eta^\ell > 0) + N\,(\Delta\eta^\ell < 0)}, \tag{2}$$

where $\Delta\eta^\ell = |\eta_\ell| - |\eta_{\bar{\ell}}|$ is the difference between the absolute pseudorapidities of the leptons that originate from the top quark ($|\eta_\ell|$) and top antiquark ($|\eta_{\bar{\ell}}|$), respectively.

Reference [9] gives a comparison of NLO QCD matrix elements (MEs) matched to parton shower (PS) calculations of the top-quark-based and leptonic charge asymmetries of $t\bar{t}$ and $t\bar{t}W$ production in the full phase space at $\sqrt{s}$ = 13 TeV. The charge asymmetry for $t\bar{t}W$ is larger than for $t\bar{t}$ production at the expense of a smaller cross-section for the process. In addition to being sensitive to BSM physics, such as axigluons and Standard Model Effective Field Theory (SMEFT) scenarios corresponding to four-fermion operators (examples given in Refs. [9] and [11]), charge asymmetry measurements have the potential to discriminate between new physics signals with different chiral structures that would be indistinguishable using only cross-section observables.

At the Tevatron, forward–backward asymmetries in $t\bar{t}$ production have been measured, with results found to be in agreement with SM calculations that include higher-order corrections [12, 13]. The ATLAS and CMS collaborations performed measurements of the top-quark-based charge asymmetry for $t\bar{t}$ production. A combination of these ATLAS and CMS results at $\sqrt{s}$ = 7 TeV and 8 TeV for the top-quark-based charge asymmetry is reported in Ref. [14] and updated measurements have been published by ATLAS and CMS using $\sqrt{s}$ = 13 TeV data [15, 16]. The measurements reported by CMS in Ref. [17] include an extraction of the leptonic charge asymmetry for $t\bar{t}$ production in a particle-level fiducial volume. A measurement of the top-quark-based charge asymmetry for $t\bar{t}$ production in association with a photon has been reported by ATLAS in Ref. [18]. None of these measurements show significant deviations from the SM expectations. In Ref. [10], NLO QCD calculations of A^ℓ_c have been performed including top-quark off-shell effects, which also include the impact of different renormalisation and factorisation scale choices on A^ℓ_c in the multi-lepton channel at the LHC at $\sqrt{s}$ = 13 TeV.[2]

This paper presents a search for the leptonic charge asymmetry in $t\bar{t}W$ production using pp collision data at $\sqrt{s}$ = 13 TeV in the trilepton (3ℓ) channel with the full Run 2 data sample, corresponding to an integrated

---

[2] These results are given in terms of the rapidities of the leptons ($A^\ell_{\mathrm{c},y}$) and not the pseudorapidities.

luminosity of 139 fb^{-1}. The paper is organised as follows. Section 2 provides a brief description of the ATLAS detector. In Section 3, the data sample as well as the simulated signal and background processes are discussed. The reconstructed particle candidates are defined in Section 4. Section 5 gives an overview of the event selection and of the definitions of the control and signal regions. The algorithm used to identify reconstructed leptons originating from top quarks (antiquarks) is explained in Section 6. In Section 7, the sources of systematic uncertainties that affect the search are discussed. The result for the charge asymmetry measurement at reconstruction level is presented in Section 8. The unfolding procedure and the extraction of the charge asymmetry at particle level are presented in Section 9. In Section 10, the conclusions are drawn.

2 The ATLAS detector

The ATLAS detector [19] at the LHC covers nearly the entire solid angle around the collision point. It consists of an inner tracking detector surrounded by a thin superconducting solenoid, electromagnetic and hadronic calorimeters, and a muon spectrometer incorporating three sets of large superconducting toroidal magnets, each consisting of eight separate coils. The inner-detector system is immersed in a 2 T axial magnetic field and provides charged-particle tracking in the range $|\eta| < 2.5$.

The high-granularity silicon pixel detector covers the vertex region and typically provides four measurements per track, with the first hit typically being detected in the insertable B-layer installed before Run 2 [20, 21]. It is followed by the silicon microstrip tracker, which usually provides eight measurements per track. These silicon detectors are complemented by the transition radiation tracker (TRT), which enables radially extended track reconstruction up to $|\eta| = 2.5$. The TRT also provides electron identification information based on the fraction of hits above a higher energy-deposit threshold corresponding to transition radiation. Typically, around 30 TRT hits are measured in total per track.

The calorimeter system covers the pseudorapidity range $|\eta| < 4.9$. In the region $|\eta| < 3.2$, electromagnetic calorimetry is provided by barrel and endcap high-granularity lead/liquid-argon (LAr) calorimeters, with an additional thin LAr presampler covering $|\eta| < 1.8$ to correct for energy loss in material upstream of the calorimeters. Hadronic calorimetry is provided by the steel/scintillator-tile calorimeter, segmented into three barrel structures with $|\eta| < 1.7$, and two copper/LAr hadronic endcap calorimeters. The solid angle coverage is extended with forward copper/LAr and tungsten/LAr calorimeter modules optimised for electromagnetic and hadronic measurements respectively.

The muon spectrometer comprises separate trigger and high-precision tracking chambers measuring the deflection of muons in a magnetic field generated by the superconducting air-core toroids. The field integral of the toroids ranges between 2.0 and 6.0 Tm across most of the detector. A set of precision chambers covers the region $|\eta| < 2.7$ with three layers of monitored drift tubes, complemented by cathode-strip chambers in the forward region, where the background rates are highest. The muon trigger system covers the range $|\eta| < 2.4$ with resistive-plate chambers in the barrel, and thin-gap chambers in the endcap regions.

Relevant events are selected to be recorded by the first-level trigger system implemented in custom hardware, followed by selections made by algorithms implemented in software in the high-level trigger [22]. The first-level trigger accepts events from the 40 MHz bunch crossings at a rate below 100 kHz, which the high-level trigger reduces to record events to disk at about 1 kHz.

An extensive software suite [23] is used in data simulation, in the reconstruction and analysis of real and simulated data, in detector operations, and in the trigger and data acquisition systems of the experiment.

3 Data and simulated event samples

The analysis is performed on data from pp collisions at $\sqrt{s} = 13$ TeV delivered by the LHC and recorded by the ATLAS detector in the years 2015–2018. The bunch spacing for this data-taking period was 25 ns with a typical number of pp interactions per bunch crossing ('pile-up') that varies by year and LHC beam conditions and was in the range from 10 to 70 for almost all events. After requirements on the stability of the beams, the operational status of all ATLAS detector components, and the quality of the recorded data, the total integrated luminosity of the data sample corresponds to 139 fb^{-1}. This value is derived from the calibration of the luminosity scale using x–y beam-separation scans, following a methodology similar to that detailed in Ref. [24], and using the LUCID-2 detector [25] for the baseline luminosity measurements.

Simulated Monte Carlo (MC) samples are used to model the contributions from the various SM processes. The MC generators used for the hard-scattering, as well as the PS, underlying event and hadronisation, are explained in the following. For some processes, in addition to the nominal simulation, alternative MC samples are available that are used to evaluate the effects of different MC modelling uncertainties (see Section 7.2). All MC samples were generated using a 25 ns bunch-spacing configuration.

The effect of pile-up was modelled by overlaying the hard-scattering event with simulated minimum-bias events generated with Pythia 8.186 [26] using the NNPDF2.3lo [27] set of parton distribution functions (PDFs) and the A3 set of tuned MC parameters [28]. Separate MC production campaigns were used to model the different pile-up distributions observed in data for the years 2015/16, 2017 and 2018. The simulated samples were reweighted to reproduce the observed distribution of the average number of collisions per bunch crossing. The simulation of detector effects was performed with either a full ATLAS detector simulation based on the Geant4 [29] framework or a fast simulation (AtlFast-II) using a parameterisation of the performance of the electromagnetic and hadronic calorimeters and Geant4 for the other detector components [30].

The signal process ($t\bar{t}W$) was simulated at NLO precision in QCD with Sherpa 2.2.10 [31] and the NNPDF3.0nnlo PDF set [32]. In this set-up, multiple MEs were matched and merged with the Sherpa PS model based on the Catani–Seymour dipole factorisation scheme [33, 34]. The virtual QCD corrections for MEs at NLO accuracy were provided by the OpenLoops library [35, 36]. Up to one additional parton was included in the NLO ME, and two, three or four additional partons were included at LO in QCD. The merging scale parameter (μ_q), which sets a threshold to determine what part of the phase-space is filled by the PS or the ME generator, was set to an energy of 30 GeV. Additional partons beyond ME-level accuracy and below the merging scale threshold were therefore described by the PS. The masses of the top quark and the W boson were set to 172.5 GeV and 80.4 GeV, respectively [37]. In addition to the nominal prediction at NLO in QCD (order of $\alpha\alpha_\text{s}^3$),[3] higher-order corrections related to EW $t\bar{t}W$ contributions were also added as part of the signal definition. The α^3 and $\alpha^2\alpha_\text{s}^2$ corrections were added through MC event weights derived using the virtual additive corrections in the formalism described in Ref. [38].

An alternative $t\bar{t}W$ sample uses MadGraph5_aMC@NLO 2.9.3 [39, 40] (in the following denoted by MG5_aMC@NLO) for the ME and was interfaced to Pythia 8.245 [41] for the PS, underlying event and hadronisation modelling. This sample was generated with the FxFx algorithm [42] with up to one

---

[3] α and α_s denote the EW and strong coupling constants, respectively.

additional parton at NLO accuracy and up to two additional partons at LO accuracy in QCD. The expected accuracy of this sample is similar to that of the nominal Sherpa 2.2.10 sample. This multi-leg configuration makes use of complex functional forms for the renormalisation and factorisation scales (μ_{r} and μ_{f}) that are chosen dynamically and depend on the kinematics of the event after the merging of the core process with the additional partons following the FxFx merging prescription [42–44]. They depend on the phase-space configuration and are related to the clustering scales of the additional partons and on the core process. The merging scale parameter was set to 30 GeV. The sample was simulated using the NNPDF3.0nlo PDF set and the A14 set of tuned MC parameters [45], henceforth referred to as the 'A14 MC tune'. Top-quark decays were simulated at LO using the MadSpin program [46, 47]. Further alternative $t\bar{t}W$ samples were simulated with the Powheg [48] generator providing ME calculations at NLO in α_{s} with the NNPDF3.0nlo PDF set and the A14 MC tune. These Powheg $t\bar{t}W$ samples were interfaced either with Pythia 8.245 or with Herwig 7.2.1 [49–51] for the simulation of the PS, underlying event and hadronisation. All the alternative $t\bar{t}W$ samples were normalised to the same cross-section as the nominal Sherpa 2.2.10 sample in order not to be sensitive to overall normalisation differences when comparing the two simulations.

The $t\bar{t}W$ EW corrections at the order of $\alpha^3\alpha_{\text{s}}$ were simulated by an independent Sherpa 2.2.10 sample, produced at LO in QCD with the same configuration as the nominal signal sample. Since the charge asymmetry from these processes is negligible compared to the nominal signal contribution, this MC sample is treated as a background in the analysis.

The production of a $t\bar{t}$ pair in association with a Z boson ($t\bar{t}Z$) was simulated at NLO precision with the MG5_aMC@NLO 2.8.1 generator for the ME and Pythia 8.244 for the PS, underlying event and hadronisation, together with the NNPDF3.0nlo PDF set and the A14 MC tune. The mass of the Z boson was set to 91.2 GeV [37]. The $t\bar{t}\gamma^*$ contribution and Z/γ^* interference effects were taken into account, with the samples including events with dilepton invariant masses ($m_{\ell\ell}$) down to 1 GeV, where ℓ is an electron or muon. Additional $t\bar{t}Z$ samples using MG5_aMC@NLO 2.8.1 for the ME, but Herwig 7.2.1 for the PS along with the Herwig standard set of tuned parameters and the NNPDF3.0nlo PDF set were used for the evaluation of systematic uncertainties associated with the PS and hadronisation. Further alternative $t\bar{t}Z$ samples with the same settings as the nominal samples, but using the A14 eigentune variation Var3c [45], are used to evaluate the uncertainty associated with the initial-state radiation (ISR). Similarly to $t\bar{t}W$, the alternative $t\bar{t}Z$ samples were normalised to the same cross-section as the nominal sample.

The production of $t\bar{t}$, $t\bar{t}H$ and tW events was simulated at NLO with the Powheg generator for the ME, together with the NNPDF3.0nlo PDF set and the A14 MC tune. The h_{damp} parameter, which controls the matching in Powheg and regulates the high-p_{T} radiation against which the $t\bar{t}$ system recoils, was set to 1.5 times the nominal top-quark mass. The events were interfaced to Pythia 8.230 for the PS, underlying event and hadronisation. The $t\bar{t}$ cross-section was normalised to next-to-next-to-leading-logarithmic order (NNLL) in QCD, including the resummation of NNLL soft-gluon terms (NNLO + NNLL) [52, 53]. The $t\bar{t}H$ samples were normalised to NLO (QCD and EW) using the calculations documented in Ref. [54]. The tW sample was normalised to NLO in QCD including NNLL soft-gluon corrections [55]. An alternative $t\bar{t}$ simulation was used with the same set-up for the ME, but the events were interfaced to Herwig 7.1.3 [56] for the PS, underlying event and hadronisation modelling. The Herwig standard set of tuned parameters and the NNPDF3.0nlo PDF set were used. Alternative $t\bar{t}H$ samples were used, where either the ME generator (MG5_aMC@NLO 2.6.0) or the PS algorithm (Herwig 7.2.1) was changed with respect to the nominal $t\bar{t}H$ simulation.

A MC sample featuring the production of $t\bar{t}$ events in association with photons ($t\bar{t}\gamma$) was simulated at LO in QCD with MG5_aMC@NLO 2.3.3 and interfaced to Pythia 8.212, together with the NNPDF3.0nlo PDF set and the A14 MC tune. This sample is, however, only used to assign an extra uncertainty to additional photon radiation in the nominal $t\bar{t}$ prediction. Details of this procedure can be found in Section 7.2.

The production of a single top quark (or antiquark) in association with a Z boson and one extra parton (tZq) was simulated using the MG5_aMC@NLO 2.3.3 generator at NLO with the NNPDF3.0nnlo PDF set. The events were interfaced to Pythia 8.245 using the A14 MC tune. The tZq simulation also includes off-shell Z boson decays into dilepton pairs with invariant masses in the range $m_{\ell\ell} > 5$ GeV. Single top quark (antiquark) production in association with both a W and a Z boson (tWZ) was simulated at NLO with MG5_aMC@NLO 2.2.2 and the NNPDF3.0nnlo PDF set, using Pythia 8.235 for the PS simulation. The interference between $t\bar{t}Z$ and tWZ was removed following a diagram-removal (DR) approach referred to as the 'DR1 scheme' [57].

The MC samples featuring Z + jets production were simulated at NLO with the Powheg generator for the ME and interfaced to Pythia 8.186 for the PS. The AZNLO [58] set of tuned parameters and the NNPDF3.0nnlo PDF set were used. An alternative Z + jets simulation was done with the Sherpa 2.2.11 generator where the default Sherpa PS set-up was used along with the NNPDF3.0nnlo PDF set. The Z + jets samples feature events with $m_{\ell\ell}$ down to 10 GeV. The sample cross-sections were normalised to NNLO predictions [59]. The Powheg + Pythia 8 sample used Photos [60] for final-state radiation (FSR).

For the simulation of Z boson production in association with a photon ($Z\gamma$), Sherpa 2.2.11 was used with the NNPDF3.0nnlo PDF set. The events were simulated at NLO precision.

Diboson processes featuring the production of three charged leptons and one neutrino or four charged leptons (denoted by WZ + jets or ZZ + jets, respectively) were simulated using the Sherpa 2.2.2 generator, with a similar set-up to that described for Z + jets. Events with up to one extra parton were simulated at NLO, and with two or three partons at LO precision. MC samples featuring Higgs boson production in association with a W or Z boson ($H + W/Z$) were generated at NLO using Powheg interfaced to Pythia 8.230/8.235 for the PS, together with the NNPDF3.0nlo PDF set and the AZNLO MC tune.

The production of four top quarks ($t\bar{t}t\bar{t}$) was modelled at NLO with Sherpa 2.2.11 together with the NNPDF3.0nnlo PDF set. The production of three top quarks ($tt\bar{t}$) and the production of a $t\bar{t}$ pair with two W bosons ($t\bar{t}WW$) were simulated at LO using MG5_aMC@NLO 2.2.2 interfaced to Pythia 8.186 with the A14 MC tune and the NNPDF2.3lo PDF set. Fully leptonically decaying triboson processes (WWW, WWZ, WZZ and ZZZ) with up to six leptons in the final states were simulated with Sherpa 2.2.2 and the NNPDF3.0nlo PDF set. Final states with no additional partons were calculated at NLO, whereas final states with one, two or three additional partons were calculated at LO.

For all MC samples except the Sherpa ones, the decays of b- and c-hadrons were simulated using the EvtGen 1.2.0 program [61].

4 Event reconstruction

Electron candidates are reconstructed from clusters of energy deposits in the electromagnetic calorimeter that are matched to tracks in the inner detector. They are required to satisfy $p_{\mathrm{T}} > 10$ GeV, $|\eta| < 2.47$ and need to pass a 'Tight' working point (WP), defined by a likelihood-based electron identification (ID) requirement [62]. To reject non-prompt electrons, the reconstructed track associated with the electron must satisfy the requirements $|z_0 \sin(\theta)| < 0.5$ mm and $|d_0|/\sigma(d_0) < 5$, where z_0 describes the longitudinal impact parameter relative to the reconstructed primary vertex,[4] d_0 is the transverse impact parameter relative to the beam axis, and $\sigma(d_0)$ is the uncertainty in d_0. Electron candidates are excluded if their calorimeter energy clusters lie within $1.37 < |\eta| < 1.52$, the transition region between the barrel and the endcap of the electromagnetic calorimeter.

Additional requirements are applied to the electron candidates to suppress the contribution of electrons originating from converted photons (γ-conversions). Electrons can be identified as internal- or material-conversion candidates by checking for additional tracks close to the calorimeter energy clusters associated with the electrons and the existence of conversion vertices. Electrons that are identified as either internal- or material-conversion candidates are rejected. These requirements are referred to in the following as 'e/γ ambiguity requirements'.

Furthermore, the electrons selected for the signal regions (SRs) of the analysis have to satisfy an isolation requirement. An isolation WP is defined using a multivariate likelihood discriminant that combines electromagnetic shower shapes and track information from the inner detector to distinguish prompt electrons from non-prompt/fake electrons originating from hadronic jets, γ-conversions and heavy-flavour hadron decays. The electrons satisfying the isolation requirements are henceforth referred to as *tight* electrons, whereas *loose* electrons are defined by the conditions listed in the previous paragraph and do not need to satisfy the isolation requirement.

Muon candidates have to satisfy $p_T > 10$ GeV, $|\eta| < 2.5$ and an ID selection, corresponding to a 'Medium' WP. This sets requirements on the number of hits in the different inner detector and muon spectrometer subsystems and on the significance of the charge-to-momentum ratio (q/p) [63, 64]. If a muon has insufficient momentum resolution, the entire event is removed. Requirements on the impact parameters of the reconstructed track associated with the muon candidate are applied to reject non-prompt muons. The track is required to have $|z_0 \sin(\theta)| < 0.5$ mm and $|d_0|/\sigma(d_0) < 3$.

As with electrons, an isolation requirement is applied to the muons used in the SRs, using the same approach based on a multivariate likelihood discriminant to distinguish prompt muons from non-prompt/fake muons. Muons are referred to as *tight* or *loose*, depending on whether or not they satisfy this isolation requirement in addition to the criteria listed above.

Jets are reconstructed using the anti-k_t jet algorithm [65] on particle-flow objects [66] with the radius parameter set to $R = 0.4$, as implemented in the FastJet package [67]. The anti-k_t algorithm is used to reconstruct jets with a four-momentum recombination scheme, using the particle-flow objects as inputs. The jet calibration is performed using a standard procedure that corrects the jet energy to match, on average, the particle-level jet energy in simulation and applies an in situ correction for data [68]. To suppress jets from additional pp interactions within the same bunch crossing, a 'jet vertex tagger' (JVT) [69, 70] is applied to select jets. The jets are only kept if they have $p_T > 20$ GeV and are in a pseudorapidity range of $|\eta| < 2.5$. In addition, JVT > 0.2 is required for jets with $p_T < 60$ GeV and $|\eta| < 2.4$, corresponding to a 'Medium' JVT WP.

The selection of jets containing b-hadrons ('b-tagging') is performed with a multivariate deep-learning algorithm referred to as `DL1r` [71, 72]. A selection that provides a 77% efficiency for identifying jets containing b-hadrons ('b-jets') in simulated $t\bar{t}$ events, with a rejection factor of 130 against light-flavour jets and of five against jets containing c-hadrons, is used.

---

[4] The primary vertex is defined as the vertex (at least two associated tracks with $p_T > 500$ MeV) with the highest scalar sum of the squared transverse momenta of the associated tracks.

Associated scale factors are applied as multiplicative factors to the MC event weights, to correct for the mis-modelling of efficiencies associated with the reconstruction, identification, isolation and trigger selection of electrons and muons, as well as the JVT and b-tagging selection for jets.

The missing transverse momentum is defined as the negative vector sum of the transverse momenta of all selected and calibrated particle candidates (electrons, muons and jets). Low-momentum tracks from the primary vertex that are not associated with any of the reconstructed particle candidates described previously are also included as a 'soft term' in the calculation [73]. The magnitude of the missing transverse momentum vector is denoted by $E_{\mathrm{T}}^{\mathrm{miss}}$.

Ambiguities between independently reconstructed electrons, muons and jets can arise. A sequential procedure, referred to as 'overlap removal', is performed to resolve these ambiguities and, thus, avoids double counting of particle candidates. It is applied as follows. if an electron candidate and a muon candidate share a track, the electron candidate is removed. Jet candidates within a distance of $\Delta R_{y,\phi} = \sqrt{(\Delta y)^2 + (\Delta\phi)^2} = 0.2$ from a remaining electron candidate are discarded. If multiple jets are found in this area, only the closest jet is removed. If the electron–jet distance is between 0.2 and 0.4, the electron candidate is removed. If the $\Delta R_{y,\phi}$ between any remaining jet and a muon candidate is less than 0.4, the muon candidate is removed if the jet has more than two associated tracks, otherwise, the jet is discarded.

5 Event selection and definitions of control and signal regions

Events were selected with either single-lepton or dilepton (dielectron, dimuon and electron–muon) triggers with their minimum p_{T} thresholds varying from 12 to 26 GeV, depending on the lepton flavour, the trigger type and the data-taking period [74, 75]. A logical 'OR' between the triggers was applied. Only events with exactly three charged light leptons (electrons or muons), as defined in Section 4, are selected. If additional *tight* electrons or muons are found in the event, the event is rejected. The transverse momenta of the three charged leptons have to be larger than 30, 20 and 15 GeV for the leading, sub-leading and third lepton, respectively. A geometrical matching between the selected leptons found in the event and the ones reconstructed by the trigger algorithms is required. Furthermore, the p_{T} of the lepton that fires a trigger needs to be above the p_{T} threshold of the respective trigger to ensure that the trigger is maximally efficient.

The selected events are classified into four SRs, depending on their jet and b-jet multiplicities, as well as their $E_{\mathrm{T}}^{\mathrm{miss}}$. In addition, four control regions (CRs) are defined to constrain the dominant backgrounds in the simultaneous fit to extract the result. In $t\bar{t}W$ production with three charged leptons in the final state, two jets originated from b-quarks are expected from the hard-process. However, additional jet activity due to gluon radiation and showering effects can occur. Thus, events are split into 'low-N_{jets}' regions with two or three jets and 'high-N_{jets}' with at least four jets.

The definitions of the SRs and CRs are summarised in Table 1. The sum of the three lepton charges must be ± 1. A requirement that the invariant mass of the opposite-sign–same-flavour lepton pair ($m_{\ell\ell}^{\mathrm{OSSF}}$) be at least 30 GeV is applied to remove the contributions from low-mass lepton resonances (e.g. $J/\psi \to \ell^+\ell^-$). The number of Z boson candidates ($N_{Z\text{-cand.}}$) is defined by the number of OSSF lepton pairs found in the event that have an invariant mass in the range $[m_Z - 10\,\mathrm{GeV}, m_Z + 10\,\mathrm{GeV}]$. Exactly one Z boson candidate is required for the CR for the $t\bar{t}Z$ background, but zero for all the other regions. The CRs targeting non-prompt electron/muons arising from heavy-flavour (HF) hadron decays (CR-HF$_e$ and CR-HF$_\mu$) are separated by the flavour of the third lepton. The third lepton must fail the isolation requirements in order to enrich these regions with HF leptons. The CR for γ-conversions (CR-γ-conv) requires at least one of the leptons to be an electron candidate that fails the e/γ ambiguity requirements defined in Section 4. The contribution from electrons with misidentified electric charge has been studied in MC and found to be negligible in the SRs.

Although the SR with two b-jets and low jet multiplicity (SR-2b-lowN_{jets}) is the most sensitive to $t\bar{t}W$ production, the best result can be obtained from a statistical combination of all SRs and CRs (see Section 8).

Table 1: Summary of the requirements applied to define the signal and control regions of the analysis. N_{jets} includes b-tagged and non-b-tagged jets. The labels ‘T’ and ‘$\overline{\text{T}}$’ refer to *tight* leptons that satisfy all selection requirements described in Section 4 (T) and *loose* leptons that fail to satisfy the isolation requirements ($\overline{\text{T}}$).

	Preselection			
N_ℓ ($\ell = e/\mu$)	$= 3$			
p_{T}^{ℓ} ($1^{\text{st}}/2^{\text{nd}}/3^{\text{rd}}$)	≥ 30 GeV, ≥ 20 GeV, ≥ 15 GeV			
Sum of lepton charges	± 1			
$m_{\ell\ell}^{\text{OSSF}}$	≥ 30 GeV			
	Region-specific requirements			
	SR-1b-lowN_{jets}	**SR-1b-highN_{jets}**	**SR-2b-lowN_{jets}**	**SR-2b-highN_{jets}**
N_{jets}	$[2, 3]$	≥ 4	$[2, 3]$	≥ 4
$N_{b\text{-jets}}$	$= 1$	$= 1$	≥ 2	≥ 2
$E_{\text{T}}^{\text{miss}}$	≥ 50 GeV	≥ 50 GeV	–	–
$N_{Z\text{-cand.}}$	$= 0$			
Lepton criteria	TTT			
e/γ ambiguity-cuts	satisfy all			
	CR-$t\bar{t}Z$	**CR-HF$_e$**	**CR-HF$_\mu$**	**CR-γ-conv**
$\ell^{1\text{st}/2\text{nd}/3\text{rd}}$	$\ell\ell\ell$	$\ell\ell e$	$\ell\ell\mu$	$\ell\ell e$, $\ell e\ell$, $e\ell\ell$
N_{jets}	≥ 4	≥ 2	≥ 2	≥ 2
$N_{b\text{-jets}}$	≥ 2	$= 1$	$= 1$	≥ 1
$E_{\text{T}}^{\text{miss}}$	–	< 50 GeV	< 50 GeV	< 50 GeV
$N_{Z\text{-cand.}}$	$= 1$	$= 0$	$= 0$	$= 0$
Lepton criteria	TTT	$\text{TT}\overline{\text{T}}$	$\text{TT}\overline{\text{T}}$	TTT
e/γ ambiguity-cuts	satisfy all	satisfy all	satisfy all	≥ 1 fail

6 Lepton–top-quark matching

In the $t\bar{t}W$ process, the leptonic charge asymmetry is calculated only from the charged leptons that originate from the top quark and top antiquark. Since this search targets events with three charged leptons, a problem arises when selecting the two leptons used to calculate the difference between their absolute pseudorapidities ($\Delta\eta^{\ell}$) and ultimately the A_{c}^{ℓ} value (as defined in Eq. (2)). The leptons that originate from a $t\bar{t}$ pair always have opposite-sign charges. In a $t\bar{t}W$ event with three charged leptons, the two leptons with the same charge cannot both come from the $t\bar{t}$ pair and will always contain one lepton from a top-quark or top-antiquark decay and one lepton from the decay of the W boson produced in association with the $t\bar{t}$ pair. This same-sign pair of leptons is henceforth referred to as the ‘even’ leptons. The remaining lepton with opposite charge, referred to as the ‘odd’ lepton, will always originate from a top quark or top antiquark. The problem of selecting the two leptons from top quark or top-antiquark decays is hence reduced to selecting one of the even leptons to calculate $\Delta\eta^{\ell}$.

This problem is addressed using a boosted decision tree (BDT) classifier algorithm that computes a discriminator value for each even lepton in each event. Large discriminator values correspond to large probabilities that a given lepton originated from a top-quark decay. The lepton with the highest BDT discriminator score is selected to calculate $\Delta\eta^{\ell}$. The $\Delta\eta^{\ell}$ values calculated with the selected lepton and the odd lepton are denoted by $\Delta\eta^{\ell}_{\mathrm{BDT}}$. Five input variables that each discriminate between leptons from top-quark or top-antiquark decays and leptons from associated W boson decays are defined. They are the masses of the two systems formed from the lepton and the closest and second closest b-jets, as well as the angular distances between the lepton and these b-jets: $m_{\ell b_0}$, $m_{\ell b_1}$, $\Delta R_{\ell b_0}$, $\Delta R_{\ell b_1}$. The last variable is the lepton p_{T}. For events with only one b-tagged jet, if any of the remaining jets pass a looser `DL1r` WP with respect to the default selection described in Section 4, the jet with the highest `DL1r` score is selected. If none of the other jets pass any b-tagging WP, the variables are constructed with the closest untagged jet.

The training of the classifier is performed using the nominal $t\bar{t}W$ SHERPA MC sample. The BDT classifier is implemented using the SCIKIT-learn [76] package. A k-fold cross validation with five folds is used for the training and testing samples. The fraction of events in the $t\bar{t}W$ sample in which the even lepton with the highest BDT discriminator value originates from a top-quark or top-antiquark decay is estimated to be about 71%, using the information from the MC event record.

7 Systematic uncertainties in background and signal estimation

The predictions of the $t\bar{t}W$ signal and the SM backgrounds are, in addition to the statistical uncertainties of their corresponding MC samples, affected by several sources of experimental and theoretical systematic uncertainty. These uncertainties are classified into the different categories that are described in the following.

7.1 Detector-related uncertainties

Detector-related uncertainties include the simulation of pile-up events, the integrated luminosity, and effects related to the reconstruction and ID of the particle candidates used in the analysis.

The uncertainty in the combined 2015–2018 integrated luminosity is 1.7% [24], obtained using the LUCID-2 detector [25] for the primary luminosity measurements. This systematic uncertainty affects all processes modelled using MC simulations apart from the processes where the associated normalisation factors are obtained from data in the simultaneous fit (see Section 8).

Uncertainties in the lepton reconstruction, ID, isolation and trigger efficiencies [62, 63, 77], electron energy and muon momentum scale and resolution [62, 63] are considered. Uncertainties associated with jets arise from the jet energy scale (JES), the jet energy resolution (JER) and the JVT jet selection requirement [68].

In addition, uncertainties associated with the pile-up rejection [69], the scale and resolution of the $E_{\mathrm{T}}^{\mathrm{miss}}$ [73], and the b-tagging efficiencies [71, 78, 79] are considered.

7.2 Signal and background modelling uncertainties

Different sources of systematic uncertainty in the theoretical predictions of the $t\bar{t}W$ signal are considered. To evaluate the effect of μ_{r} and μ_{f} uncertainties, the scale factors used in the ME of the Sherpa $t\bar{t}W$ sample are varied simultaneously, as well as individually, by factors of 2.0 and 0.5 relative to their nominal values (but not including combinations where the variations differ by a factor of four). Uncertainties associated with the PDF sets are evaluated according to the PDF4LHC prescription [80]. They include internal variations of the nominal PDF sets that are added in quadrature, uncertainties due to the choice of PDF set, as well as variations of the α_{s} parameter. The systematic uncertainties due to the modelling of the ME are evaluated by comparing the prediction of the nominal MC sample with that of an alternative $t\bar{t}W$ sample simulated with MG5_aMC@NLO + Pythia and the FxFx algorithm. Furthermore, to evaluate the systematic uncertainties due to the PS, the hadronisation and the underlying event, the $t\bar{t}W$ Powheg + Pythia samples are compared with the Powheg + Herwig samples and their relative differences are applied as uncertainties in the nominal Sherpa prediction. As explained in Section 3, the alternative samples employed for the evaluation of modelling uncertainties are normalised to the same cross-sections as the respective nominal samples, so that the systematic uncertainties cover only differences between the shapes of kinematic variable distributions, but not the overall normalisations of the processes.

For the theoretical systematic uncertainties in the $t\bar{t}Z$ background, the same prescriptions as for the $t\bar{t}W$ process are used to evaluate the effects of the μ_{r} and μ_{f} uncertainties. For the systematic uncertainties due to the PS, the hadronisation and the underlying event, the nominal $t\bar{t}Z$ prediction is compared with that of an alternative $t\bar{t}Z$ sample simulated with the same ME generator (MG5_aMC@NLO), but interfaced to Herwig instead of Pythia. Further alternative $t\bar{t}Z$ samples using a set of variations of the A14 tune's parameters are used to evaluate the uncertainty associated with the ISR, as mentioned in Section 3.

For the $t\bar{t}H$, tZq and $WZ/ZZ+$jets backgrounds, μ_{r} and μ_{f} uncertainties are considered. To evaluate the uncertainty in the ME, the PS, the hadronisation and the underlying event of $t\bar{t}H$, the nominal prediction is compared with those from the alternative $t\bar{t}H$ MC samples that use either a different ME generator (MG5_aMC@NLO) or PS algorithm (Herwig). Furthermore, a normalisation uncertainty of $+5.8\%$ and -9.2% is applied for $t\bar{t}H$, following the NLO (QCD + EW) calculations from Ref. [54]. For the tZq process, a normalisation uncertainty of 14% is applied, based on the dedicated ATLAS tZq measurement described in Ref. [81]. For the $WZ/ZZ+$jets backgrounds, a conservative normalisation uncertainty of 20% is used to account for differences in the quality of $WZ/ZZ+$jets modelling for different b-jet multiplicities. This uncertainty is derived from the level of agreement between data and MC simulation in several validation regions enriched in $WZ/ZZ+$jets.

For the $t\bar{t}$ and $Z+$jets backgrounds, which can only contribute to 3ℓ final states via the presence of an additional fake or non-prompt lepton, μ_{r} and μ_{f} uncertainties are also considered. For the $t\bar{t}$ process, the PS, the hadronisation and the underlying event uncertainties are evaluated by comparing the nominal MC sample (Powheg + Pythia) with an equivalent $t\bar{t}$ sample with the same ME generator, but interfaced to Herwig. An extra uncertainty associated with the photon radiation in $t\bar{t}$ events is applied by comparing the predictions from $t\bar{t}$ and $t\bar{t} + t\bar{t}\gamma$.[5] For $Z+$jets, the uncertainties in the ME, the PS, the hadronisation and the underlying event are evaluated from a comparison between the nominal MC samples (Powheg + Pythia) and alternative $Z+$jets ($Z\gamma$) samples, which are simulated with Sherpa. The same approach as for $t\bar{t}$ is followed to account for the uncertainty associated with the photon radiation in $Z+$jets events.

For the other (minor) background processes (tW, tWZ, $t\bar{t}WW$, $H+W/Z$, VVV ($V = W/Z$), $tt\bar{t}$ and $t\bar{t}t\bar{t}$), which typically contribute less than 2% to the total event yields in the SRs, a normalisation uncertainty of 30% is applied. This is a conservative approach, which should cover the known theoretical uncertainties of these backgrounds. The same also applies to the MC sample generated with $t\bar{t}W$ EW corrections at the order $\alpha^3\alpha_\mathrm{s}$, as this is treated as a background (see Section 3).

8 Extraction of the charge asymmetry at reconstruction level

To extract the leptonic charge asymmetry from the reconstructed leptons (detector level), a simultaneous fit to the numbers of observed events in the SRs and CRs, as defined in Section 5, is performed. The fit is based on the profile-likelihood technique, with a binned likelihood function defined as a product of Poisson probabilities of the observed event yields in all the regions. Systematic uncertainties (see Section 7) are taken into account in the likelihood function, each as a nuisance parameter constrained by a Gaussian probability density function [82].

The normalisation factors for the most relevant background processes in the SRs, namely $t\bar{t}Z$, non-prompt electrons/muons from HF decays and electrons from γ-conversions, are allowed to float freely in the fit. Events containing non-prompt leptons from HF decays and electrons from γ-conversions are selected from processes that cannot contribute directly to the 3ℓ final state: $t\bar{t}$, tW and $Z+$jets. These events are identified by requiring at least one lepton to originate from either a b/c-hadron ($\mathrm{HF}_{e/\mu}$) or a converted photon (γ-conversion) according to the MC event records of the selected leptons. The variables used as input to the binned likelihood fit are the p_T of the third (softest) lepton in CR-HF_e and CR-HF_μ, as well as the H_T in CR-$t\bar{t}Z$,[6] since their distributions show a sizeable shape difference between the targeted processes and the other SM backgrounds. In the SRs and CR-γ-conv, the total numbers of events are used.

Each of the four SRs is separated into $\Delta\eta^\ell_\mathrm{BDT} \leq 0$ ($\Delta\eta^-$) and $\Delta\eta^\ell_\mathrm{BDT} > 0$ ($\Delta\eta^+$) regions. For the $\Delta\eta^-$ ($\Delta\eta^+$) set of regions, a single factor $\mathcal{N}_{\Delta\eta^-}$ ($\mathcal{N}_{\Delta\eta^+}$) models the normalisations of the signal yields (relatively to the SM cross-section) across the four SRs. Accordingly, the A^ℓ_c value is extracted as a function of these normalisation factors. Similarly, separate normalisation factors in the $\Delta\eta^-$ and $\Delta\eta^+$ sets of regions for the major background processes are allowed to float freely in the fit to avoid a bias from an assumption of SM asymmetries for these processes in data.[7] An 'injection test' is performed to verify that the fit result matches an injected non-SM A^ℓ_c value and the fit can deal correctly with the fact that the different SRs have different charge asymmetries.

The predicted and observed numbers of events in the SRs and CRs before performing the simultaneous fit ('pre-fit') are given in Table 2. The indicated uncertainties consider statistical as well as all experimental and theoretical systematic uncertainties described in Section 7. The numbers of events in the SRs and

---

[5] The overlap between the photons radiated within the PS in the $t\bar{t}$ ($Z+$jets) simulation and the photons coming from $t\bar{t}\gamma$ ($Z\gamma$) is removed from $t\bar{t}$ ($Z+$jets) for this comparison. This is done at particle level, where final-state photons that do not originate from prompt particle decays are removed if they are inside the kinematic phase-space covered by the $t\bar{t}\gamma$ ($Z\gamma$) simulation.

[6] The H_T is defined as the scalar sum of the p_T of the selected jets in the event.

[7] The inclusive charge asymmetries at parton level for the simulated $t\bar{t}Z$ and $t\bar{t}$ samples are $A^\ell_\mathrm{c} = -0.015$ and 0.004, respectively.

CRs after the fit to data ('post-fit') are given in Table 3. Comparisons between data and the post-fit SM predictions for the variables that are used for the binned likelihood fit are given in Figure 2 for CR-HF$_e$ and CR-HF$_\mu$, and in Figure 3 for CR-$t\bar{t}Z$ and CR-γ-conv. The data and the post-fit predictions for $\Delta\eta^-$ and $\Delta\eta^+$ in the four SRs are shown in Figure 4.

Table 2: The predicted and observed numbers of events in the control and signal regions. The predictions are shown before the fit to data. The indicated uncertainties consider statistical as well as all experimental and theoretical systematic uncertainties. Background categories with event yields shown as '—' do contribute less than 0.01 to a region.

Process	CR-$t\bar{t}Z$		CR-HF$_e$		CR-HF$_\mu$		CR-γ-conv	
	$\Delta\eta^-$	$\Delta\eta^+$	$\Delta\eta^-$	$\Delta\eta^+$	$\Delta\eta^-$	$\Delta\eta^+$	$\Delta\eta^-$	$\Delta\eta^+$
$t\bar{t}W$ (QCD)	1.8 ± 0.4	1.49 ± 0.19	1.18 ± 0.19	1.13 ± 0.18	1.72 ± 0.20	1.37 ± 0.28	4.1 ± 0.7	2.92 ± 0.18
$t\bar{t}W$ (EW)	0.18 ± 0.07	0.16 ± 0.06	0.10 ± 0.04	0.09 ± 0.04	0.09 ± 0.04	0.14 ± 0.05	0.23 ± 0.08	0.36 ± 0.12
$t\bar{t}Z$	107 ± 6	107 ± 6	1.42 ± 0.23	1.5 ± 0.4	2.20 ± 0.23	2.00 ± 0.14	4.04 ± 0.19	3.65 ± 0.32
HF$_e$	–	–	350 ± 40	362 ± 27	0.18 ± 0.11	0.20 ± 0.09	1.0 ± 0.6	0.67 ± 0.35
HF$_\mu$	0.14 ± 0.08	0.19 ± 0.09	0.20 ± 0.09	0.28 ± 0.10	520 ± 40	530 ± 50	0.9 ± 0.5	1.1 ± 0.9
γ-conv.	0.55 ± 0.14	0.41 ± 0.13	3.8 ± 2.5	4.7 ± 2.9	2.6 ± 2.4	3.3 ± 2.5	18.8 ± 1.4	17.5 ± 1.3
$t\bar{t}H$	3.3 ± 0.4	3.20 ± 0.32	0.87 ± 0.13	0.89 ± 0.11	1.18 ± 0.11	1.22 ± 0.22	1.48 ± 0.20	1.5 ± 0.4
tZq	12.6 ± 2.2	11.0 ± 1.9	0.48 ± 0.11	0.43 ± 0.09	0.95 ± 0.18	0.81 ± 0.15	0.68 ± 0.12	0.70 ± 0.13
WZ/ZZ + jets	12 ± 4	12 ± 4	3.0 ± 0.9	3.3 ± 1.0	7.2 ± 2.4	7.9 ± 2.5	3.1 ± 0.9	2.9 ± 0.8
Other	10.7 ± 3.3	10.2 ± 3.3	14 ± 4	13 ± 5	17 ± 7	17 ± 6	1.6 ± 0.8	1.5 ± 0.6
SM total	148 ± 10	146 ± 10	380 ± 40	387 ± 28	550 ± 40	560 ± 50	35.9 ± 2.4	32.9 ± 2.3
Data	156	176	315	373	551	592	34	40

Process	SR-1b-lowN_{jets}		SR-1b-highN_{jets}		SR-2b-lowN_{jets}		SR-2b-highN_{jets}	
	$\Delta\eta^-$	$\Delta\eta^+$	$\Delta\eta^-$	$\Delta\eta^+$	$\Delta\eta^-$	$\Delta\eta^+$	$\Delta\eta^-$	$\Delta\eta^+$
$t\bar{t}W$ (QCD)	19 ± 3	17 ± 4	9.2 ± 1.1	8.2 ± 1.1	25 ± 7	21 ± 6	14.7 ± 3.4	12.2 ± 1.9
$t\bar{t}W$ (EW)	1.06 ± 0.34	1.3 ± 0.4	1.05 ± 0.34	1.07 ± 0.34	1.2 ± 0.4	1.3 ± 0.4	1.8 ± 0.6	1.6 ± 0.5
$t\bar{t}Z$	12.0 ± 1.0	12.1 ± 1.1	15.5 ± 1.4	15.5 ± 1.1	11.4 ± 1.4	10.8 ± 1.4	26.2 ± 1.8	25.8 ± 1.7
HF$_e$	7.2 ± 1.2	7.5 ± 1.5	1.7 ± 0.7	1.6 ± 0.6	0.7 ± 0.5	0.6 ± 0.5	0.69 ± 0.35	0.37 ± 0.19
HF$_\mu$	12.5 ± 2.0	13 ± 4	3.2 ± 0.8	3.5 ± 1.3	1.35 ± 0.34	1.11 ± 0.33	1.0 ± 0.4	0.9 ± 0.5
γ-conv.	6.7 ± 0.9	6.1 ± 1.0	3.1 ± 0.5	3.4 ± 0.8	6.1 ± 0.8	6.9 ± 0.8	4.4 ± 0.7	4.6 ± 0.6
$t\bar{t}H$	5.5 ± 0.8	5.6 ± 0.8	8.6 ± 0.8	8.7 ± 0.9	5.5 ± 1.1	5.5 ± 1.0	14.1 ± 1.8	14.2 ± 1.7
tZq	5.1 ± 0.9	4.2 ± 0.7	1.40 ± 0.31	1.15 ± 0.27	2.8 ± 0.5	2.3 ± 0.4	1.92 ± 0.34	1.64 ± 0.30
WZ/ZZ + jets	15 ± 4	14 ± 4	8.0 ± 2.8	7.6 ± 2.5	2.9 ± 0.9	2.2 ± 0.7	2.2 ± 0.7	2.2 ± 0.7
Other	5.6 ± 2.0	5.1 ± 1.6	4.5 ± 2.4	4.7 ± 1.5	2.6 ± 1.1	2.9 ± 1.3	10 ± 6	9 ± 5
SM total	89 ± 6	85 ± 7	56 ± 6	56 ± 6	59 ± 9	55 ± 7	77 ± 8	73 ± 7
Data	94	89	50	69	84	81	89	81

The normalisation factors for the major background processes, $\mathcal{N}_{t\bar{t}Z}$, $\mathcal{N}^{e}_{\gamma\text{-conv}}$, $\mathcal{N}^{e}_{\text{HF}}$ and $\mathcal{N}^{\mu}_{\text{HF}}$ (all obtained separately for $\Delta\eta^-$ and $\Delta\eta^+$), together with $\mathcal{N}_{\Delta\eta^-}$ and the A^{ℓ}_{c} value for the $t\bar{t}W$ signal, are given in Figure 5. The normalisation factor for the $t\bar{t}W$ process was checked and found to be (within its uncertainty) compatible with the latest ATLAS and CMS $t\bar{t}W$ cross-section measurements [7, 8]. Tests using MC simulation were also performed to validate that the extracted A^{ℓ}_{c} value is not biased by the absolute normalisation of the $t\bar{t}W$ process.

The normalisation factors for some of the background processes (in particular $\mathcal{N}_{t\bar{t}Z}$ and $\mathcal{N}^{e}_{\gamma\text{-conv}}$) show small differences between $\Delta\eta^-$ and $\Delta\eta^+$. As these processes are not expected to have significant charge

Table 3: The predicted and observed numbers of events in the control and signal regions. The predictions are shown after the fit to data. The indicated uncertainties consider statistical as well as all experimental and theoretical systematic uncertainties. Background categories with event yields shown as '—' do contribute less than 0.01 to a region.

Process	CR-$t\bar{t}Z$		CR-HF$_e$		CR-HF$_\mu$		CR-γ-conv	
	$\Delta\eta^-$	$\Delta\eta^+$	$\Delta\eta^-$	$\Delta\eta^+$	$\Delta\eta^-$	$\Delta\eta^+$	$\Delta\eta^-$	$\Delta\eta^+$
$t\bar{t}W$ (QCD)	3.2 ± 0.7	2.2 ± 0.7	1.8 ± 0.5	1.7 ± 0.5	2.6 ± 0.8	1.8 ± 0.8	7.0 ± 1.3	4.4 ± 1.3
$t\bar{t}W$ (EW)	0.18 ± 0.06	0.16 ± 0.05	0.10 ± 0.03	0.09 ± 0.03	0.09 ± 0.03	0.14 ± 0.04	0.23 ± 0.07	0.36 ± 0.11
$t\bar{t}Z$	114 ± 13	138 ± 14	1.45 ± 0.27	1.7 ± 0.4	2.3 ± 0.4	2.55 ± 0.35	4.3 ± 0.6	4.6 ± 0.6
HF$_e$	–	–	290 ± 18	346 ± 20	0.15 ± 0.02	0.19 ± 0.02	0.59 ± 0.27	0.52 ± 0.17
HF$_\mu$	0.13 ± 0.01	0.20 ± 0.02	0.20 ± 0.02	0.28 ± 0.03	516 ± 25	556 ± 25	0.8 ± 0.4	1.3 ± 0.8
γ-conv.	0.40 ± 0.18	0.52 ± 0.16	2.8 ± 2.2	6 ± 4	1.9 ± 2.0	4.2 ± 3.4	14 ± 6	22 ± 7
$t\bar{t}H$	3.3 ± 0.4	3.23 ± 0.31	0.86 ± 0.13	0.87 ± 0.10	1.16 ± 0.11	1.19 ± 0.22	1.49 ± 0.20	1.6 ± 0.4
tZq	12.6 ± 2.2	11.0 ± 1.9	0.47 ± 0.10	0.42 ± 0.08	0.95 ± 0.17	0.79 ± 0.14	0.68 ± 0.11	0.70 ± 0.12
WZ/ZZ + jets	10.2 ± 2.9	10.6 ± 3.1	2.6 ± 0.7	2.8 ± 0.7	6.3 ± 1.7	6.7 ± 1.8	2.6 ± 0.7	2.5 ± 0.6
Other	10.8 ± 3.2	10.0 ± 2.9	14 ± 4	13 ± 5	18 ± 7	18 ± 6	1.7 ± 0.8	1.7 ± 0.6
SM total	155 ± 12	175 ± 13	315 ± 18	373 ± 19	550 ± 23	591 ± 24	33 ± 6	40 ± 6
Data	156	176	315	373	551	592	34	40

Process	SR-1b-lowN_{jets}		SR-1b-highN_{jets}		SR-2b-lowN_{jets}		SR-2b-highN_{jets}	
	$\Delta\eta^-$	$\Delta\eta^+$	$\Delta\eta^-$	$\Delta\eta^+$	$\Delta\eta^-$	$\Delta\eta^+$	$\Delta\eta^-$	$\Delta\eta^+$
$t\bar{t}W$ (QCD)	32 ± 6	27 ± 6	14 ± 4	12.1 ± 3.4	46 ± 9	36 ± 8	26 ± 6	19 ± 5
$t\bar{t}W$ (EW)	1.04 ± 0.32	1.3 ± 0.4	1.04 ± 0.32	1.05 ± 0.32	1.2 ± 0.4	1.3 ± 0.4	1.8 ± 0.5	1.6 ± 0.5
$t\bar{t}Z$	12.4 ± 2.0	15.0 ± 2.2	16.0 ± 2.2	19.6 ± 2.3	12.3 ± 2.3	14.3 ± 2.6	27.6 ± 3.3	33.2 ± 3.5
HF$_e$	6.4 ± 1.0	6.8 ± 0.8	1.5 ± 0.5	1.7 ± 0.4	0.40 ± 0.20	0.79 ± 0.35	0.45 ± 0.14	0.39 ± 0.14
HF$_\mu$	12.5 ± 1.5	13.6 ± 2.5	3.1 ± 0.6	3.6 ± 0.9	1.30 ± 0.23	1.19 ± 0.19	1.04 ± 0.29	0.9 ± 0.5
γ-conv.	4.9 ± 2.3	7.7 ± 2.6	2.3 ± 1.1	4.3 ± 1.6	4.6 ± 2.1	8.8 ± 2.9	3.3 ± 1.5	5.9 ± 1.9
$t\bar{t}H$	5.4 ± 0.8	5.5 ± 0.8	8.4 ± 0.8	8.6 ± 0.8	5.5 ± 1.1	5.6 ± 1.0	14.3 ± 1.7	14.4 ± 1.7
tZq	5.0 ± 0.9	4.1 ± 0.7	1.38 ± 0.27	1.16 ± 0.24	2.8 ± 0.5	2.3 ± 0.4	1.93 ± 0.33	1.65 ± 0.29
WZ/ZZ + jets	12.6 ± 3.0	12.3 ± 3.0	6.7 ± 2.0	6.5 ± 1.8	2.5 ± 0.7	1.9 ± 0.5	1.9 ± 0.6	1.9 ± 0.5
Other	6.0 ± 2.1	5.2 ± 1.6	3.6 ± 1.8	4.6 ± 1.4	2.9 ± 1.2	3.3 ± 1.3	8 ± 4	8 ± 4
SM total	99 ± 6	98 ± 6	58 ± 4	63 ± 4	80 ± 8	75 ± 7	85 ± 6	86 ± 5
Data	94	89	50	69	84	81	89	81

asymmetries in the SM at this level of precision, there is an uncertainty on how best to model this data. In the nominal fit, due to the independent normalisation factors for $\Delta\eta^-$ and $\Delta\eta^+$ in the CRs, the observed background asymmetries are precisely modelled. To account for the possibility that the observed asymmetry is due to a systematic effect, an alternative fit is performed where only one normalisation factor is assigned to each of these processes (thus fixing their asymmetries to the SM expectation). The difference between the results of these two fit set-ups is assigned as an extra systematic uncertainty in the extracted A_c^ℓ value. This uncertainty (denoted as $\Delta\eta^\pm$ CR-dependency) is found to be 0.046 and is one of the leading systematic uncertainties.

The leptonic charge asymmetry in $t\bar{t}W$ is found to be

$$A_\text{c}^\ell(t\bar{t}W) = -0.123 \pm 0.136\,(\text{stat.}) \pm 0.051\,(\text{syst.}),$$

This is consistent with the SM expectation of

$$A_{\mathrm{c}}^{\ell}(t\bar{t}W)_{\mathrm{SM}} = -0.084\,^{+0.005}_{-0.003}\,(\mathrm{scale}) \pm 0.006\,(\mathrm{MC\ stat.}),$$

calculated using the nominal $t\bar{t}W$ Sherpa simulation. The contributions from the most relevant uncertainties are summarised in Table 4. The uncertainties are symmetrised and grouped into several type-related categories and are shown together with the total systematic and statistical uncertainties. The dominant systematic uncertainties are the $\Delta\eta^{\pm}$ CR-dependency, the JER, as well as the modelling uncertainties of the $t\bar{t}W$ and $t\bar{t}Z$ MC processes detailed in Section 7. Overall, the result is limited by the statistical uncertainty of the data.

Table 4: List of the most relevant systematic and statistical uncertainties in the extracted leptonic charge asymmetry $A_{\mathrm{c}}^{\ell}(t\bar{t}W)$ from the simultaneous fit. For this table, the uncertainties are symmetrised and grouped into categories. The sum in quadrature of the individual uncertainties is not necessarily equal to the total uncertainty due to correlations introduced by the fit.

	$\Delta A_{\mathrm{c}}^{\ell}(t\bar{t}W)$
Experimental uncertainties	
Jet energy resolution	0.013
Pile-up	0.007
b-tagging	0.005
Leptons	0.004
$E_{\mathrm{T}}^{\mathrm{miss}}$	0.004
Jet energy scale	0.003
Luminosity	0.001
MC modelling uncertainties	
$t\bar{t}W$ modelling	0.013
$t\bar{t}Z$ modelling	0.010
$\mathrm{HF}_{e/\mu}$ modelling	0.006
$t\bar{t}H$ modelling	0.005
Other uncertainties	
$\Delta\eta^{\pm}$ CR-dependency	0.046
MC statistical uncertainty	0.019
Data statistical uncertainty	0.136
Total uncertainty	0.145

9 Unfolding and extraction of the charge asymmetry at particle level

To obtain the charge asymmetry at particle level in a specific fiducial volume, an unfolding procedure is performed to correct for detector effects, as well as for signal efficiency and acceptance effects. The procedure and the relevant definitions are explained in the following.

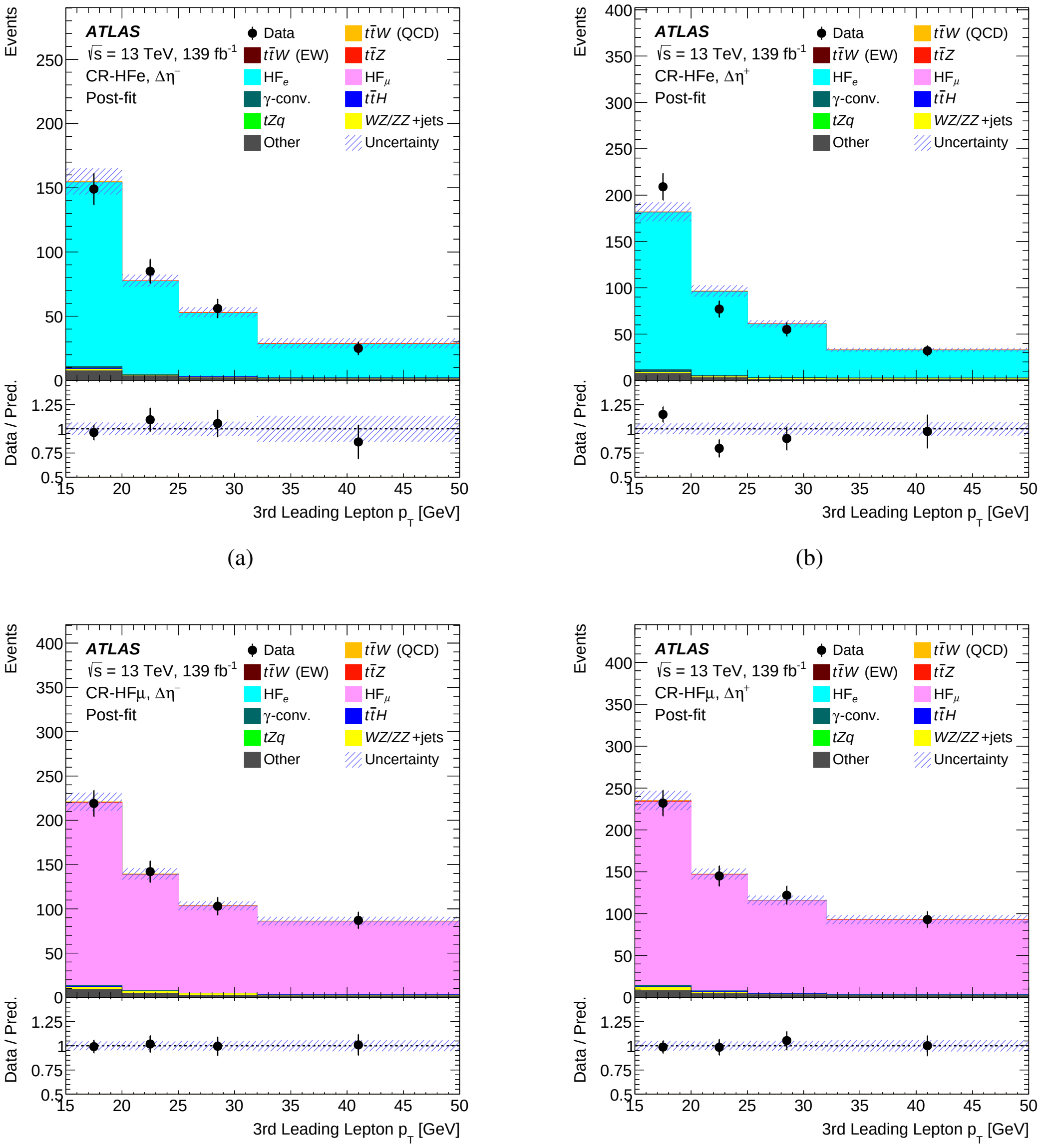

(a) (b)

(c) (d)

Figure 2: Comparison between data and the post-fit predictions in (a,b) CR-HF$_e$ and (c,d) CR-HF$_\mu$. The distributions show the p_T of the third lepton (electron or muon), which is the variable that is used for the binned likelihood fit. The regions are separated between $\Delta\eta^{\ell}_{\mathrm{BDT}} \leq 0$ ($\Delta\eta^{-}$) and $\Delta\eta^{\ell}_{\mathrm{BDT}} > 0$ ($\Delta\eta^{+}$). The error bands include the total uncertainties in the post-fit predictions. The ratios of the data to the total post-fit predictions are shown in the lower panels. Events with the p_T of the third lepton above 50 GeV are included in the rightmost bins.

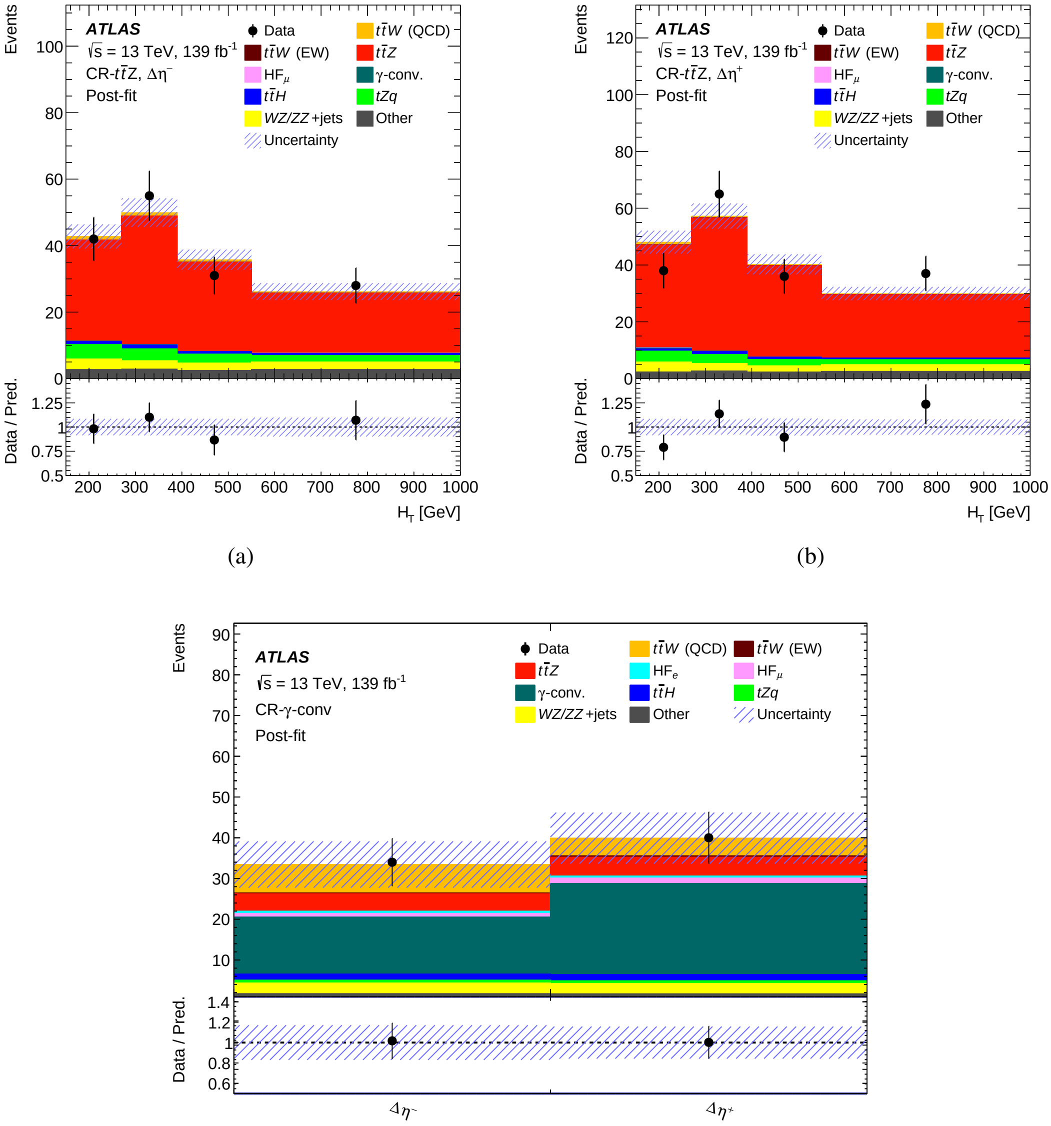

(a)

(b)

(c)

Figure 3: Comparison between data and the post-fit predictions in (a,b) CR-$t\bar{t}Z$ and (c) CR-γ-conv. The distributions are shown for the variables that are used for the binned likelihood fit: H_{T} for CR-$t\bar{t}Z$ and the total event yields for CR-γ-conv. The regions are separated between $\Delta\eta^{\ell}_{\mathrm{BDT}} \leq 0$ ($\Delta\eta^{-}$) and $\Delta\eta^{\ell}_{\mathrm{BDT}} > 0$ ($\Delta\eta^{+}$). The error bands include the total uncertainties in the post-fit predictions. The ratios of the data to the total post-fit predictions are shown in the lower panels. Events with an H_{T} above 1 TeV are included in the rightmost bins of (a) and (b).

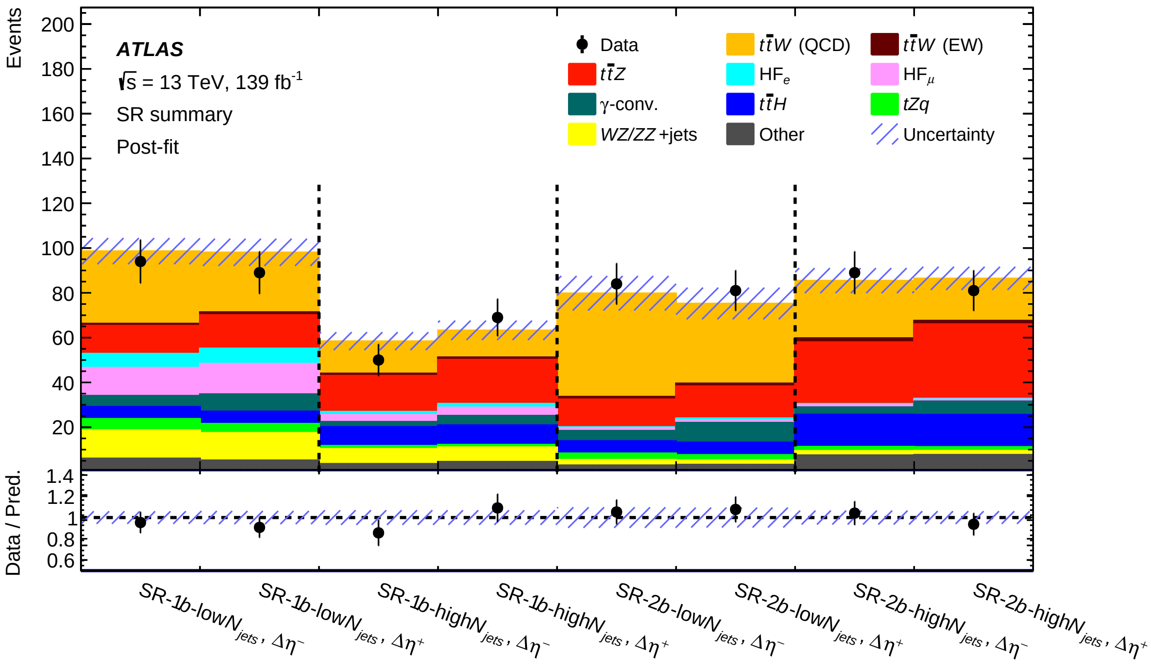

Figure 4: Comparison between data and the post-fit predictions for $\Delta\eta^{\ell}_{\mathrm{BDT}} \leq 0$ ($\Delta\eta^{-}$) and $\Delta\eta^{\ell}_{\mathrm{BDT}} > 0$ ($\Delta\eta^{+}$) in the four SRs. The error band includes the total uncertainties of the post-fit predictions. The ratio of the data to the total post-fit predictions is shown in the lower panel.

9.1 Particle-level objects

Particle-level objects in simulated events are defined using quasi-stable particles (with a mean lifetime greater than 30 ps) originating from pp collisions. They are selected after hadronisation but before the interaction with the various detector components or consideration of pile-up effects.

Particle-level electrons or muons are required to not originate from a hadron in the MC generator event record, whether directly or through a τ-lepton decay. This ensures that they originate from a Z or W boson (where the W boson can come either from prompt W production or a top-quark decay), without requiring a direct match with the parent particle. The four-momenta of the bare leptons are modified (‘dressed’) by adding the four-momenta of all radiated photons within a cone of size $\Delta R = 0.1$, excluding photons from hadron decays, to take into account FSR photons.

Particle-level jets are reconstructed with the anti-k_t algorithm with a radius parameter of $R = 0.4$ applied to all stable particles, but excluding the neutrinos originating from W or Z bosons and the selected electrons, muons and photons used in the definition of the charged leptons. If b-hadrons with $p_{\mathrm{T}} > 5$ GeV are found in the MC event record, they are clustered into stable-particle jets with their energies set to negligible positive values (referred to as ‘ghost-matching’) [83]. Particle-level jets containing at least one of these b-hadrons are considered as b-jets. The particle-level missing transverse momentum is defined as the vectorial sum of the transverse momenta of all neutrinos found in the MC simulation history of the event, excluding those originating from hadron decays.

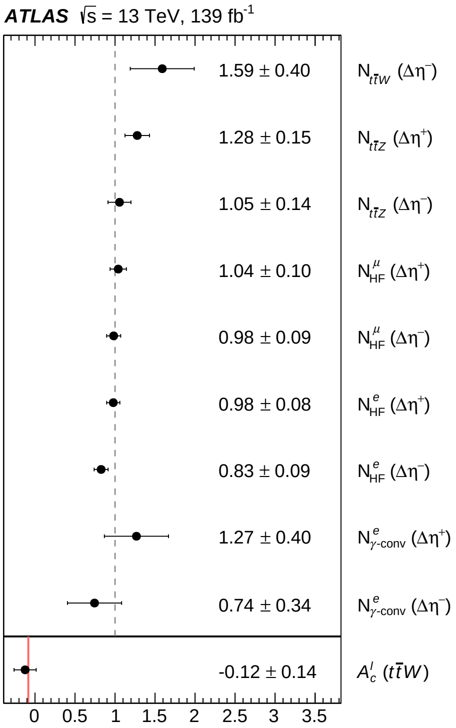

Figure 5: Normalisation factors for the major background processes, together with $\mathcal{N}_{\Delta\eta^-}$ for $t\bar{t}W$ and the A_c^ℓ value extracted from the fit to data in the CRs and SRs. The normalisation factors, $\mathcal{N}_{t\bar{t}Z}$, $\mathcal{N}^e_{\gamma\text{-conv}}$, $\mathcal{N}^e_\text{HF}$ and $\mathcal{N}^\mu_\text{HF}$, are obtained separately for $\Delta\eta^\ell_\text{BDT} \leq 0$ ($\Delta\eta^-$) and $\Delta\eta^\ell_\text{BDT} > 0$ ($\Delta\eta^+$). The indicated uncertainties consider statistical as well as systematic uncertainties. The solid vertical line in the last entry shows the A_c^ℓ SM expectation, calculated using the $t\bar{t}W$ Sherpa simulation.

9.2 Particle-level fiducial volume

The particle-level fiducial volume is defined by the following requirements on the particle-level objects, as defined in Section 9.1:

- Three electrons or muons with $p_\text{T} > 15$ GeV and $|\eta| < 2.5$.
- The invariant mass of all OSSF lepton pairs has to be larger than 25 GeV.
- No Z-candidate (as defined in Section 5) among the leptons.
- At least two jets with $p_\text{T} > 20$ GeV, $|\eta| < 2.5$ and least one of them identified as a b-jet.

9.3 Unfolding procedure and charge-asymmetry extraction

The unfolding procedure is applied to the observed number of data events in the SRs. Analogously to the method used at detector level, described in Section 6, a method of matching leptons to top quarks (antiquarks) is required to obtain the response matrix, essential to the unfolding procedure. To reproduce the particle-level fiducial volume, a simpler scheme is adopted that is independent of the generator-specific MC event record and any multivariate algorithm. Each lepton is combined with the closest b-jet in the ΔR space. The ℓ–b system that yields a mass closest to the most probable mass for a ℓ–b system originating from a top-quark decay (according to the nominal $t\bar{t}W$ simulation) is used to select the even and odd leptons. This procedure has an efficiency of approximately 65% to identify the correct leptons.

The following formula is used for the unfolding:

$$N_i^{\text{folded}} = \underbrace{\frac{1}{\alpha_i} \sum_j \varepsilon_j M_{ij}}_{R_{ij}} N_j^{\text{fid}} \quad \text{with} \quad M_{ij} = \frac{N_{ij}^{(\text{reco} \cap \text{fid})}}{N_j^{(\text{reco} \cap \text{fid})}}, \quad \alpha_i = \frac{N_i^{(\text{reco} \cap \text{fid})}}{N_i^{\text{reco}}}, \quad \varepsilon_j = \frac{N_j^{(\text{reco} \cap \text{fid})}}{N_j^{\text{fid}}}, \tag{3}$$

with the number N_j^{fid} representing the content of bin j after the unfolding procedure. The response matrix (R_{ij}) is constructed from the migration matrix (M_{ij}) and the acceptance and efficiency correction terms (α_i and ε_j) for each bin. The entries in the migration matrix represent the fractions of events at particle level in a y-axis bin that are reconstructed at detector level in an x-axis bin. They are normalised such that the sum of entries in each row is equal to one. The acceptance corrections α_i account for events that are generated outside the fiducial volume ('fid') but satisfy the selection at detector level ('reco'), as described in Section 5. The efficiency corrections ε_j account for events that are in the fiducial volume but fail to satisfy the detector-level selection. The symbol $\cap$ represents the logical intersection of the two regions.

The migration matrices, as well as the acceptance and efficiency correction terms, are built separately for each of the SRs defined in Table 1. As an example, Figure 6 shows (a) the migration matrix, as well as (b) the efficiency and (c) the acceptance correction factors that are used for SR-2b-lowN_{jets}, which is the region with the highest $t\bar{t}W$ purity. The fraction of events in the diagonal elements of the migration matrix shows the quality of the resolution for $\Delta\eta^{\ell}$, which is around 90%. The efficiency corrections are at a level of 11%–12% and the acceptance corrections are around 95%. None show any notable dependence on $\Delta\eta^{\ell}$.

The unfolding procedure is the same as in Ref. [18] and based on a profile-likelihood approach ('profile-likelihood unfolding'). With this approach, the unfolding problem is transformed into a standard problem of fitting normalisations of distributions. Each bin in the particle-level distribution is 'folded' through the response matrix via Eq. (3), resulting in the same numbers of bins at detector level. The particle-level bins are treated as separate subsamples that are multiplied by their respective entries in the response matrix and freely floating parameters are assigned to each of these subsamples at detector level. Analogously to the fit described in Section 8, the freely floating parameters are assigned to the major backgrounds in the SRs: $\mathcal{N}_{t\bar{t}Z}$, $\mathcal{N}^{e}_{\gamma\text{-conv}}$, $\mathcal{N}^{e}_{\text{HF}}$ and $\mathcal{N}^{\mu}_{\text{HF}}$. These normalisations and the analysis regions are split into $\Delta\eta^{+}$ and $\Delta\eta^{-}$, in the same way as the detector-level results. Thus, the detector-level distributions are scaled by some factors, determined by fitting the data, and these factors are then used to scale the corresponding particle-level bins, which gives the desired unfolded result. The charge asymmetry is defined as the parameter of interest and is related to the normalisation factors in the unfolded bins. For the CRs, no response matrices are built. However, as the signal contamination in these regions is very small compared with the total event yields, an approximation is made whereby the signal is treated as an additional background. An exception is CR-γ-conv where, due to the high signal contamination, response matrices are also built. No regularisation is applied in the unfolding.

The systematic uncertainties in the signal and background processes considered for the unfolded results are the same as for the results at detector level (described in Section 7). Systematic uncertainties in the

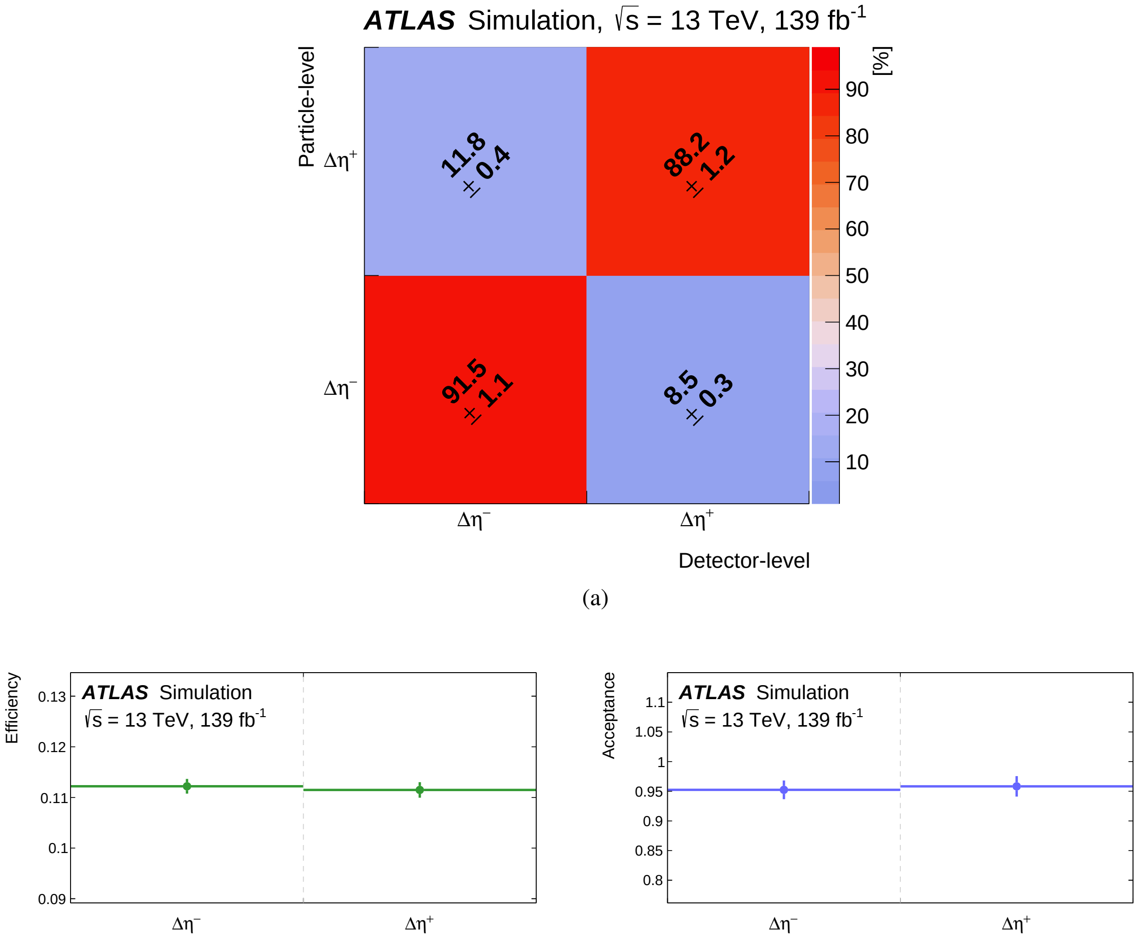

(a)

(b)

(c)

Figure 6: (a) The migration matrix and (b,c) the efficiency/acceptance corrections that are used as input for the unfolding of SR-2b-lowN_{jets}. The matrices are normalised such that the sum of any given row is 100%, although small differences may be present due to rounding. The error bars of the efficiency/acceptance correction terms represent the MC statistical uncertainties per bin based on the nominal $t\bar{t}W$ Sherpa sample.

background processes are propagated to the unfolded distributions by varying the detector-level distributions within their uncertainties and repeating the unfolding procedure. The modelling uncertainties of the $t\bar{t}W$ signal are propagated through the unfolding procedure, using variations of the response matrices.

An injection test is performed to verify that non-SM A_{c}^{ℓ} values can be recovered in the unfolding procedure. This is done by injecting the non-SM A_{c}^{ℓ} values into the particle-level predictions, which are propagated to detector level and treated as pseudo-data in the fit. The unfolding procedure is then performed on this pseudo-data for several positive and negative deviations from the SM A_{c}^{ℓ} to compute the relation between the injected and extracted A_{c}^{ℓ} values and to estimate the bias that the fit procedure introduces. After the fit to real data, the observed A_{c}^{ℓ} is substituted into the relation to extract the bias. The bias estimated from this procedure is found to be 0.004. Although this value is well covered by the systematic uncertainties, it is added as an extra uncertainty in the unfolded A_{c}^{ℓ} value to account for this effect.

The charge asymmetry value, unfolded to particle level (PL) in the fiducial volume defined in Section 9.2, is found to be

$$A_{\mathrm{c}}^{\ell}(t\bar{t}W)^{\mathrm{PL}} = -0.112 \pm 0.170\,(\text{stat.}) \pm 0.054\,(\text{syst.}),$$

with a SM expectation calculated using the nominal $t\bar{t}W$ Sherpa simulation of

$$A_{\mathrm{c}}^{\ell}(t\bar{t}W)_{\mathrm{SM}}^{\mathrm{PL}} = -0.063\,^{+0.007}_{-0.004}\,(\text{scale}) \pm 0.004\,(\text{MC stat.}).$$

The nominal values for the background normalisations are the same as reported in Section 8. The contributions from the most relevant uncertainties in the charge asymmetry at particle level are given in Table 5. The sources of uncertainty are similar to the ones reported in Table 4, with the $\Delta\eta^{\pm}$ CR-dependency, the modelling of the $t\bar{t}W$ and $t\bar{t}Z$ MC processes and the statistical uncertainty being the dominant ones. The statistical uncertainty is slightly increased relative to the detector-level result due to the unfolding procedure.

10 Conclusions

This paper presents a search for the leptonic charge asymmetry in $t\bar{t}W$ production using pp collision data at $\sqrt{s} = 13$ TeV with the full Run 2 data sample collected with the ATLAS detector at the LHC, corresponding to an integrated luminosity of 139 fb^{-1}. The leptonic charge asymmetry is defined as the pseudorapidity difference between the two reconstructed charged leptons associated with top quarks (or top antiquarks). The search is performed in 3ℓ final states using reconstructed light leptons (electrons or muons), together with jets and b-jets. To correctly match the leptons to either top quarks or top antiquarks, a technique based on a BDT is used.

The charge asymmetry at reconstruction level is obtained by performing a simultaneous profile-likelihood fit to data in different signal and control regions optimised for either the $t\bar{t}W$ process or the major SM background processes ($t\bar{t}Z$, non-prompt leptons from HF decays or electrons from γ-conversions). The charge asymmetry is extracted together with the normalisations for these background processes and is found to be

$$A_{\mathrm{c}}^{\ell}(t\bar{t}W) = -0.123 \pm 0.136\,(\text{stat.}) \pm 0.051\,(\text{syst.}).$$

This is consistent with the SM expectation of

$$A_{\mathrm{c}}^{\ell}(t\bar{t}W)_{\mathrm{SM}} = -0.084\,^{+0.005}_{-0.003}\,(\text{scale}) \pm 0.006\,(\text{MC stat.}),$$

Table 5: List of the most relevant systematic and statistical uncertainties in the leptonic charge asymmetry at particle level $A_\mathrm{c}^\ell(t\bar{t}W)^\mathrm{PL}$. For this table, the uncertainties are symmetrised and grouped into categories. The sum in quadrature of the individual uncertainties is not necessarily equal to the total uncertainty due to correlations introduced by the fit.

	$\Delta A_\mathrm{c}^\ell(t\bar{t}W)^\mathrm{PL}$
Experimental uncertainties	
Leptons	0.014
Jet energy resolution	0.011
Pile-up	0.008
Jet energy scale	0.004
$E_\mathrm{T}^\mathrm{miss}$	0.002
Luminosity	0.001
Jet vertex tagger	0.001
MC modelling uncertainties	
$t\bar{t}W$ modelling	0.022
$t\bar{t}Z$ modelling	0.017
$\mathrm{HF}_{e/\mu}$ modelling	0.015
Others modelling	0.015
$WZ/ZZ+$jets modelling	0.014
$t\bar{t}H$ modelling	0.006
Other uncertainties	
Unfolding bias	0.004
$\Delta\eta^\pm$ CR-dependency	0.039
MC statistical uncertainty	0.027
Response matrix	0.009
Data statistical uncertainty	0.170
Total uncertainty	0.179

calculated using the nominal $t\bar{t}W$ Sherpa simulation. An unfolding procedure is used to obtain the charge asymmetry at particle level in a specific fiducial volume in the 3ℓ channel. The unfolding is based on a profile-likelihood approach, where the unfolding is performed together with fitting normalisations of the major background processes, using the same procedure used to derive the charge asymmetry at reconstruction level. The charge asymmetry at particle level yields

$$A_\mathrm{c}^\ell(t\bar{t}W)^\mathrm{PL} = -0.112 \pm 0.170\,(\mathrm{stat.}) \pm 0.054\,(\mathrm{syst.}),$$

with a SM expectation calculated using the nominal $t\bar{t}W$ Sherpa simulation of

$$A_\mathrm{c}^\ell(t\bar{t}W)^\mathrm{PL}_\mathrm{SM} = -0.063\,^{+0.007}_{-0.004}\,(\mathrm{scale}) \pm 0.004\,(\mathrm{MC\ stat.}).$$

The most relevant systematic uncertainties affecting this search are the $\Delta\eta^\pm$ CR-dependency of the fit, as well as the modelling uncertainties of the $t\bar{t}W$ and $t\bar{t}Z$ MC processes in the 3ℓ channel. However, both the reconstruction- and particle-level results are severely limited by the statistical uncertainties of the data.

References

[1] A. Broggio et al., *Top-quark pair hadroproduction in association with a heavy boson at NLO+NNLL including EW corrections*, JHEP **08** (2019) 039, arXiv: `1907.04343 [hep-ph]`.

[2] B. Grzadkowski, M. Iskrzynski, M. Misiak and J. Rosiek, *Dimension-six terms in the Standard Model Lagrangian*, JHEP **10** (2010) 085, arXiv: `1008.4884 [hep-ph]`.

[3] ATLAS Collaboration, *Search for squarks and gluinos in final states with same-sign leptons and jets using 139 fb^{-1} of data collected with the ATLAS detector*, JHEP **06** (2020) 046, arXiv: `1909.08457 [hep-ex]`.

[4] ATLAS Collaboration, *Search for new phenomena in events with same-charge leptons and b-jets in pp collisions at $\sqrt{s} = 13$ TeV with the ATLAS detector*, JHEP **12** (2018) 039, arXiv: `1807.11883 [hep-ex]`.

[5] ATLAS Collaboration, *Evidence for the associated production of the Higgs boson and a top quark pair with the ATLAS detector*, Phys. Rev. D **97** (2018) 072003, arXiv: `1712.08891 [hep-ex]`.

[6] ATLAS Collaboration, *Measurement of the $t\bar{t}t\bar{t}$ production cross section in pp collisions at $\sqrt{s} = 13$ TeV with the ATLAS detector*, JHEP **11** (2021) 118, arXiv: `2106.11683 [hep-ex]`.

[7] ATLAS Collaboration, *Measurement of the $t\bar{t}Z$ and $t\bar{t}W$ cross sections in proton–proton collisions at $\sqrt{s} = 13$ TeV with the ATLAS detector*, Phys. Rev. D **99** (2019) 072009, arXiv: `1901.03584 [hep-ex]`.

[8] CMS Collaboration, *Measurement of the cross section of top quark-antiquark pair production in association with a W boson in proton-proton collisions at $\sqrt{s} = 13$ TeV*, (2022), arXiv: `2208.06485 [hep-ex]`.

[9] F. Maltoni, M. L. Mangano, I. Tsinikos and M. Zaro, *Top-quark charge asymmetry and polarization in $t\bar{t}W^{\pm}$ production at the LHC*, Phys. Lett. B **736** (2014) 252, arXiv: `1406.3262 [hep-ph]`.

[10] G. Bevilacqua et al., *NLO QCD corrections to off-shell $t\bar{t}W^{\pm}$ production at the LHC: correlations and asymmetries*, Eur. Phys. J. C **81** (2021) 675, arXiv: `2012.01363 [hep-ph]`.

[11] I. Brivio and M. Trott, *The Standard Model as an Effective Field Theory*, Phys. Rept. **793** (2019) 1, arXiv: `1706.08945 [hep-ph]`.

[12] CDF Collaboration, *Evidence for a mass dependent forward-backward asymmetry in top quark pair production*, Phys. Rev. D **83** (2011) 112003, arXiv: `1101.0034 [hep-ex]`.

[13] CDF and D0 Collaborations, *Combined forward-backward asymmetry measurements in top-antitop quark production at the Tevatron*, Phys. Rev. Lett. **120** (2018) 042001, arXiv: `1709.04894 [hep-ex]`.

[14] ATLAS and CMS Collaborations, *Combination of inclusive and differential $t\bar{t}$ charge asymmetry measurements using ATLAS and CMS data at $\sqrt{s} = 7$ and 8 TeV*, JHEP **04** (2018) 033, arXiv: `1709.05327 [hep-ex]`.

[15] ATLAS Collaboration, *Evidence for the charge asymmetry in $pp \to t\bar{t}$ production at $\sqrt{s} = 13$ TeV with the ATLAS detector*, (2022), arXiv: `2208.12095 [hep-ex]`.

[16] CMS Collaboration, *Measurement of the $t\bar{t}$ charge asymmetry in events with highly Lorentz-boosted top quarks in pp collisions at $\sqrt{s} = 13$ TeV*, (2022), arXiv: `2208.02751 [hep-ex]`.

[17] CMS Collaboration, *Measurements of $t\bar{t}$ differential cross sections in proton–proton collisions at $\sqrt{s} = 13$ TeV using events containing two leptons*, JHEP **02** (2019) 149, arXiv: `1811.06625 [hep-ex]`.

[18] ATLAS Collaboration, *Measurement of the charge asymmetry in top-quark pair production in association with a photon with the ATLAS experiment*, (2022), arXiv: `2212.10552 [hep-ex]`.

[19] ATLAS Collaboration, *The ATLAS Experiment at the CERN Large Hadron Collider*, JINST **3** (2008) S08003.

[20] ATLAS Collaboration, *ATLAS Insertable B-Layer Technical Design Report*, ATLAS-TDR-19; CERN-LHCC-2010-013, 2010, URL: `https://cds.cern.ch/record/1291633`, Addendum: ATLAS-TDR-19-ADD-1; CERN-LHCC-2012-009, 2012, URL: `https://cds.cern.ch/record/1451888`.

[21] B. Abbott et al., *Production and integration of the ATLAS Insertable B-Layer*, JINST **13** (2018) T05008, arXiv: `1803.00844 [physics.ins-det]`.

[22] ATLAS Collaboration, *Performance of the ATLAS trigger system in 2015*, Eur. Phys. J. C **77** (2017) 317, arXiv: `1611.09661 [hep-ex]`.

[23] ATLAS Collaboration, *The ATLAS Collaboration Software and Firmware*, ATL-SOFT-PUB-2021-001, 2021, URL: `https://cds.cern.ch/record/2767187`.

[24] ATLAS Collaboration, *Luminosity determination in pp collisions at $\sqrt{s} = 13$ TeV using the ATLAS detector at the LHC*, ATLAS-CONF-2019-021, 2019, URL: `https://cds.cern.ch/record/2677054`.

[25] G. Avoni et al., *The new LUCID-2 detector for luminosity measurement and monitoring in ATLAS*, JINST **13** (2018) P07017.

[26] T. Sjöstrand, S. Mrenna and P. Skands, *A brief introduction to PYTHIA 8.1*, Comput. Phys. Commun. **178** (2008) 852, arXiv: `0710.3820 [hep-ph]`.

[27] R. D. Ball et al., *Parton distributions with LHC data*, Nucl. Phys. B **867** (2013) 244, arXiv: `1207.1303 [hep-ph]`.

[28] ATLAS Collaboration, *The Pythia 8 A3 tune description of ATLAS minimum bias and inelastic measurements incorporating the Donnachie–Landshoff diffractive model*, ATL-PHYS-PUB-2016-017, 2016, URL: `https://cds.cern.ch/record/2206965`.

[29] GEANT4 Collaboration, S. Agostinelli et al., *GEANT4 – a simulation toolkit*, Nucl. Instrum. Meth. A **506** (2003) 250.

[30] ATLAS Collaboration, *The ATLAS Simulation Infrastructure*, Eur. Phys. J. C **70** (2010) 823, arXiv: `1005.4568 [physics.ins-det]`.

[31] E. Bothmann et al., *Event generation with Sherpa 2.2*, SciPost Phys. **7** (2019) 034, arXiv: `1905.09127 [hep-ph]`.

[32] R. D. Ball et al., *Parton distributions for the LHC run II*, JHEP **04** (2015) 040, arXiv: `1410.8849 [hep-ph]`.

[33] T. Gleisberg and S. Höche, *Comix, a new matrix element generator*, JHEP **12** (2008) 039, arXiv: `0808.3674 [hep-ph]`.

[34] S. Schumann and F. Krauss,
A parton shower algorithm based on Catani–Seymour dipole factorisation, JHEP **03** (2008) 038,
arXiv: `0709.1027 [hep-ph]`.

[35] F. Cascioli, P. Maierhöfer and S. Pozzorini, *Scattering Amplitudes with Open Loops*,
Phys. Rev. Lett. **108** (2012) 111601, arXiv: `1111.5206 [hep-ph]`.

[36] A. Denner, S. Dittmaier and L. Hofer,
Collier: A fortran-based complex one-loop library in extended regularizations,
Comput. Phys. Commun. **212** (2017) 220, arXiv: `1604.06792 [hep-ph]`.

[37] Particle Data Group, *Review of Particle Physics*, PTEP **2022** (2022) 083C01.

[38] S. Kallweit, J. M. Lindert, P. Maierhöfer, S. Pozzorini and M. Schönherr, *NLO QCD+EW predictions for V + jets including off-shell vector-boson decays and multijet merging*,
JHEP **04** (2016) 021, arXiv: `1511.08692 [hep-ph]`.

[39] J. Alwall, M. Herquet, F. Maltoni, O. Mattelaer and T. Stelzer, *MadGraph 5 : going beyond*,
JHEP **06** (2011) 128, arXiv: `1106.0522 [hep-ph]`.

[40] J. Alwall et al., *The automated computation of tree-level and next-to-leading order differential cross sections, and their matching to parton shower simulations*, JHEP **07** (2014) 079,
arXiv: `1405.0301 [hep-ph]`.

[41] T. Sjöstrand et al., *An introduction to PYTHIA 8.2*, Comput. Phys. Commun. **191** (2015) 159,
arXiv: `1410.3012 [hep-ph]`.

[42] R. Frederix and S. Frixione, *Merging meets matching in MC@NLO*, JHEP **12** (2012) 061,
arXiv: `1209.6215 [hep-ph]`.

[43] S. Catani, F. Krauss, B. R. Webber and R. Kuhn, *QCD Matrix Elements + Parton Showers*,
JHEP **11** (2001) 063, arXiv: `hep-ph/0109231`.

[44] K. Hamilton, P. Nason and G. Zanderighi, *MINLO: multi-scale improved NLO*,
JHEP **10** (2012) 155, arXiv: `1206.3572 [hep-ph]`.

[45] ATLAS Collaboration, *ATLAS Pythia 8 tunes to* 7 *TeV data*, ATL-PHYS-PUB-2014-021, 2014,
URL: `https://cds.cern.ch/record/1966419`.

[46] S. Frixione, E. Laenen, P. Motylinski and B. R. Webber, *Angular correlations of lepton pairs from vector boson and top quark decays in Monte Carlo simulations*, JHEP **04** (2007) 081,
arXiv: `hep-ph/0702198`.

[47] P. Artoisenet, R. Frederix, O. Mattelaer and R. Rietkerk,
Automatic spin-entangled decays of heavy resonances in Monte Carlo simulations,
JHEP **03** (2013) 015, arXiv: `1212.3460 [hep-ph]`.

[48] S. Frixione, P. Nason and C. Oleari,
Matching NLO QCD computations with parton shower simulations: the POWHEG method,
JHEP **11** (2007) 070, arXiv: `0709.2092 [hep-ph]`.

[49] G. Corcella et al., *HERWIG 6: an event generator for hadron emission reactions with interfering gluons (including supersymmetric processes)*, JHEP **01** (2001) 010, arXiv: `hep-ph/0011363`.

[50] M. Bähr et al., *Herwig++ physics and manual*, Eur. Phys. J. C **58** (2008) 639,
arXiv: `0803.0883 [hep-ph]`.

[51] J. Bellm et al., *Herwig 7.2 release note*, Eur. Phys. J. C **80** (2020) 452,
arXiv: `1912.06509 [hep-ph]`.

[52] K. Melnikov, M. Schulze and A. Scharf,
QCD corrections to top quark pair production in association with a photon at hadron colliders,
Phys. Rev. D **83** (2011) 074013, arXiv: `1102.1967 [hep-ph]`.

[53] M. Czakon and A. Mitov,
NNLO corrections to top pair production at hadron colliders: the quark-gluon reaction,
JHEP **01** (2013) 080, arXiv: `1210.6832 [hep-ph]`.

[54] D. de Florian et al.,
Handbook of LHC Higgs Cross Sections: 4. Deciphering the Nature of the Higgs Sector, (2016),
arXiv: `1610.07922 [hep-ph]`.

[55] N. Kidonakis,
Two-loop soft anomalous dimensions for single top quark associated production with a W^- *or* H^-,
Phys. Rev. D **82** (2010) 054018, arXiv: `1005.4451 [hep-ph]`.

[56] J. Bellm et al., *Herwig 7.1 Release Note*, (2017), arXiv: `1705.06919 [hep-ph]`.

[57] F. Demartin, B. Maier, F. Maltoni, K. Mawatari and M. Zaro,
tWH associated production at the LHC, Eur. Phys. J. C **77** (2017) 34,
arXiv: `1607.05862 [hep-ph]`.

[58] ATLAS Collaboration, *Measurement of the* Z/γ^* *boson transverse momentum distribution in* pp *collisions at* $\sqrt{s} = 7$ *TeV with the ATLAS detector*, JHEP **09** (2014) 145,
arXiv: `1406.3660 [hep-ex]`.

[59] K. Melnikov and F. Petriello,
Electroweak gauge boson production at hadron colliders through $O(\alpha_s^2)$,
Phys. Rev. D **74** (2006) 114017, arXiv: `hep-ph/0609070`.

[60] P. Golonka and Z. Was,
PHOTOS Monte Carlo: a precision tool for QED corrections in Z and W decays,
Eur. Phys. J. C **45** (2006) 97, arXiv: `hep-ph/0506026`.

[61] D. J. Lange, *The EvtGen particle decay simulation package*,
Nucl. Instrum. Meth. A **462** (2001) 152.

[62] ATLAS Collaboration, *Electron and photon performance measurements with the ATLAS detector using the 2015–2017 LHC proton–proton collision data*, JINST **14** (2019) P12006,
arXiv: `1908.00005 [hep-ex]`.

[63] ATLAS Collaboration, *Muon reconstruction performance of the ATLAS detector in proton–proton collision data at* $\sqrt{s} = 13$ *TeV*, Eur. Phys. J. C **76** (2016) 292, arXiv: `1603.05598 [hep-ex]`.

[64] ATLAS Collaboration, *Muon reconstruction and identification efficiency in ATLAS using the full Run 2* pp *collision data set at* $\sqrt{s} = 13$ *TeV*, Eur. Phys. J. C **81** (2021) 578,
arXiv: `2012.00578 [hep-ex]`.

[65] M. Cacciari, G. P. Salam and G. Soyez, *The anti-*k_t *jet clustering algorithm*, JHEP **04** (2008) 063,
arXiv: `0802.1189 [hep-ph]`.

[66] ATLAS Collaboration,
Jet reconstruction and performance using particle flow with the ATLAS Detector,
Eur. Phys. J. C **77** (2017) 466, arXiv: `1703.10485 [hep-ex]`.

[67] M. Cacciari, G. P. Salam and G. Soyez, *FastJet user manual*, Eur. Phys. J. C **72** (2012) 1896,
arXiv: `1111.6097 [hep-ph]`.

[68] ATLAS Collaboration, *Jet energy scale and resolution measured in proton–proton collisions at $\sqrt{s} = 13$ TeV with the ATLAS detector*, Eur. Phys. J. C **81** (2020) 689, arXiv: `2007.02645 [hep-ex]`.

[69] ATLAS Collaboration, *Tagging and suppression of pileup jets with the ATLAS detector*, ATLAS-CONF-2014-018, 2014, URL: `https://cds.cern.ch/record/1700870`.

[70] ATLAS Collaboration, *Performance of pile-up mitigation techniques for jets in pp collisions at $\sqrt{s} = 8$ TeV using the ATLAS detector*, Eur. Phys. J. C **76** (2016) 581, arXiv: `1510.03823 [hep-ex]`.

[71] ATLAS Collaboration, *ATLAS b-jet identification performance and efficiency measurement with $t\bar{t}$ events in pp collisions at $\sqrt{s} = 13$ TeV*, Eur. Phys. J. C **79** (2019) 970, arXiv: `1907.05120 [hep-ex]`.

[72] ATLAS Collaboration, *ATLAS flavour-tagging algorithms for the LHC Run 2 pp collision dataset*, (2022), arXiv: `2211.16345 [physics.data-an]`.

[73] ATLAS Collaboration, *Performance of missing transverse momentum reconstruction with the ATLAS detector using proton–proton collisions at $\sqrt{s} = 13$ TeV*, Eur. Phys. J. C **78** (2018) 903, arXiv: `1802.08168 [hep-ex]`.

[74] ATLAS Collaboration, *Performance of the ATLAS muon triggers in Run 2*, JINST **15** (2020) P09015, arXiv: `2004.13447 [hep-ex]`.

[75] ATLAS Collaboration, *Performance of electron and photon triggers in ATLAS during LHC Run 2*, Eur. Phys. J. C **80** (2020) 47, arXiv: `1909.00761 [hep-ex]`.

[76] F. Pedregosa et al., *Scikit-learn: machine learning in python*, Journal of Machine Learning Research **12** (2011) 2825, URL: `https://dl.acm.org/doi/10.5555/1953048.2078195`.

[77] ATLAS Collaboration, *Electron reconstruction and identification in the ATLAS experiment using the 2015 and 2016 LHC proton–proton collision data at $\sqrt{s} = 13$ TeV*, Eur. Phys. J. C **79** (2019) 639, arXiv: `1902.04655 [hep-ex]`.

[78] ATLAS Collaboration, *Optimisation and performance studies of the ATLAS b-tagging algorithms for the 2017-18 LHC run*, ATL-PHYS-PUB-2017-013, 2017, URL: `https://cds.cern.ch/record/2273281`.

[79] ATLAS Collaboration, *Calibration of light-flavour b-jet mistagging rates using ATLAS proton–proton collision data at $\sqrt{s} = 13$ TeV*, ATLAS-CONF-2018-006, 2018, URL: `https://cds.cern.ch/record/2314418`.

[80] J. Butterworth et al., *PDF4LHC recommendations for LHC Run II*, J. Phys. G **43** (2016) 023001, arXiv: `1510.03865 [hep-ph]`.

[81] ATLAS Collaboration, *Observation of the associated production of a top quark and a Z boson in pp collisions at $\sqrt{s} = 13$ TeV with the ATLAS detector*, JHEP **07** (2020) 124, arXiv: `2002.07546 [hep-ex]`.

[82] W. Verkerke and D. Kirkby, *The RooFit toolkit for data modeling*, 2003, arXiv: `physics/0306116 [physics.data-an]`.

[83] M. Cacciari, G. P. Salam and G. Soyez, *The catchment area of jets*, JHEP **04** (2008) 005, arXiv: `0802.1188 [hep-ph]`.